Nanoparticles that communicate *in vivo* to amplify tumour targeting

Geoffrey von Maltzahn[1,2], Ji-Ho Park[3], Kevin Y. Lin[4], Neetu Singh[1], Christian Schwöppe[5], Rolf Mesters[5], Wolfgang E. Berdel[5], Erkki Ruoslahti[6,7], Michael J. Sailor[8,9] and Sangeeta N. Bhatia[1,10,11,12]★

Nanomedicines have enormous potential to improve the precision of cancer therapy, yet our ability to efficiently home these materials to regions of disease *in vivo* remains very limited. Inspired by the ability of communication to improve targeting in biological systems, such as inflammatory-cell recruitment to sites of disease, we construct systems where synthetic biological and nanotechnological components communicate to amplify disease targeting *in vivo*. These systems are composed of 'signalling' modules (nanoparticles or engineered proteins) that target tumours and then locally activate the coagulation cascade to broadcast tumour location to clot-targeted 'receiving' nanoparticles in circulation that carry a diagnostic or therapeutic cargo, thereby amplifying their delivery. We show that communicating nanoparticle systems can be composed of multiple types of signalling and receiving modules, can transmit information through multiple molecular pathways in coagulation, can operate autonomously and can target over 40 times higher doses of chemotherapeutics to tumours than non-communicating controls.

Advances in nanotechnology have produced a diverse toolkit of individual nanodevices with unique electromagnetic properties[1–3] and the ability to encapsulate and programmably release a diversity of therapeutics[4–9], yet the ultimate biomedical efficacy of such devices largely depends on their *in vivo* fate. Over the past three decades, approaches to targeting nanomaterials *in vivo* have focused on tuning the properties of individual nanoparticles (NPs) including geometry, surface chemistry, ligand type and ligand density[10–18]. These materials are typically administered as populations of >1 trillion NPs to carry out identical, competitive functions *in vivo*. Here, inspired by the power of communication to improve targeting across multiple length scales in biological systems (for example, insect swarming, immune-cell trafficking, platelet self-assembly), we considered the design of NP systems that communicate to enhance *in vivo* diagnostics, regenerative medicines and therapeutics.
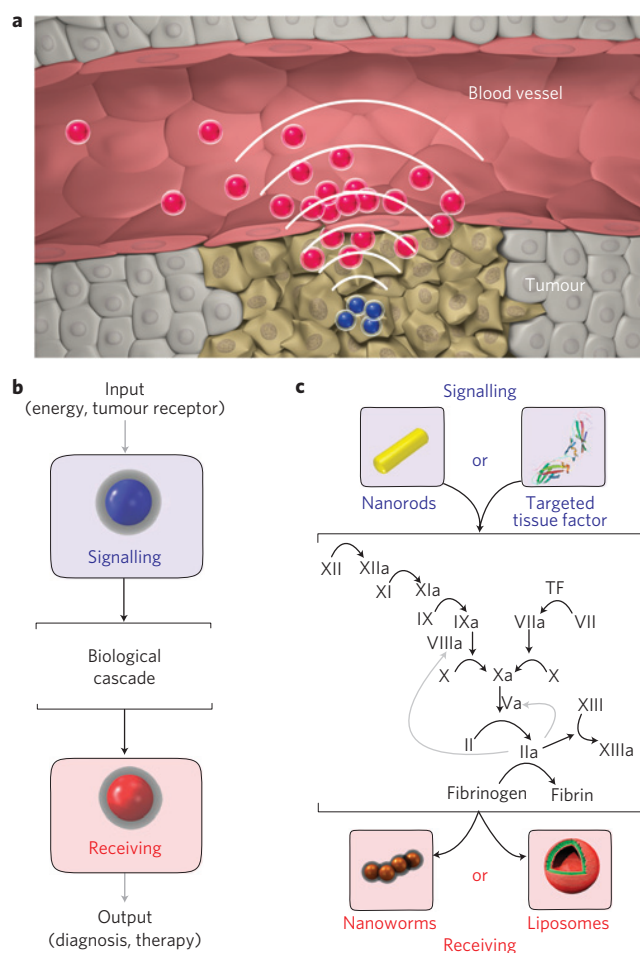
We set out to construct two-component nanosystems from well-characterized NP and biological components, wherein signalling modules would first target tumours and then broadcast the tumour's location to receiving NPs in circulation (Fig. 1a). To facilitate rapid and robust signal transmission in regions of tumour growth, we sought to harness the machinery of an endogenous multistep biological cascade to transmit communications (Fig. 1b) and selected the coagulation cascade due to its powerful signal

amplification, positive feedback, ubiquitous presence in plasma and potential to operate across multiple tumour types (Fig. 1c). We hypothesized that two signalling modules could selectively activate the coagulation cascade in tumours: NPs (gold nanorods, NRs) that target tumours and convert external electromagnetic energy into heat to locally disrupt tumour vessels, and engineered human proteins (tumour-targeted tissue factor, tTF) that autonomously survey host vessels for angiogenic tumour receptors and, in their presence, activate the extrinsic coagulation pathway (Fig. 1c).

Receiving modules were constructed using two nanomaterial platforms: a prototypical imaging agent (magnetofluorescent iron oxide nanoworms, NWs) and a prototypical therapeutic agent (doxorubicin-loaded liposomes, LPs). We explored the potential to route communication to receivers through two molecular pathways in coagulation by developing peptide coatings that recognize fibrin directly and peptides that target coagulation enzyme activity by acting as a substrate for the coagulation transglutaminase factor XIII (FXIII) (Fig. 1c).

We first set out to examine the capacity of signalling modules to precisely induce coagulation in tumours (Fig. 2a). To test our hypothesis that photothermal heating of gold NRs could disrupt tumour blood vessels to initiate extravascular coagulation[19–22], we examined the transduction of tumour heating into localized coagulation by evaluating fibrin deposition in tumours as a function

Figure 1 | Nanoparticles communication for amplified tumour targeting. a, Schematic representation of communication between system components. Tumour-targeted signalling NPs broadcast the tumour location to receiving NPs in circulation. **b**, Harnessing a biological cascade to transmit and amplify NP communications. **c**, Molecular signalling pathway between the signalling and receiving components. Signalling and receiving components act as unnatural inputs and outputs to the coagulation cascade, respectively. Signalling components are either tumour-targeted plasmonic gold NRs, which initiate coagulation cascade activation in tumours by photothermally disrupting tumour vessels and activating the extrinsic and intrinsic coagulation pathways, or tumour-targeted truncated tissue factor proteins, which are latent in circulation and activate the extrinsic coagulation pathway on binding to tumour receptors. Communication is exploited to recruit inorganic (iron oxide nanoworms) or organic (drug-loaded LPs) receiving components through activity of the coagulation transglutaminase FXIII or through targeting of polymerized fibrin.

of temperature (Fig. 2a). Purified fibrinogen (the precursor to fibrin) and albumin (an abundant blood protein unrelated to coagulation) were labelled with unique near-infrared (NIR) fluorochromes to allow simultaneous assessment of coagulation-dependent and independent protein tropism to heated tumours. Mixtures of fibrinogen and albumin were intravenously injected into athymic (*nu/nu*) mice bearing bilateral human MDA-MB-435 tumours, after which one tumour was heated using a temperature-controlled water bath. At 24 h, mice were killed and the relative levels of tumour fibrin(ogen) and albumin were assessed fluorescently. We observed a marked induction of fibrin(ogen) accumulation in tumours between 45 °C and 53 °C, with little accompanying increase in albumin accumulation, indicating

that heat specifically directed coagulation-cascade activation in tumours (Fig. 2b, Supplementary Fig. S1). Immunohistochemical staining for fibrin(ogen) in tumours from uninjected mice corroborated these findings, demonstrating that exogenous fibrinogen administration did not artificially drive accumulation in heated tumours (Supplementary Fig. S1).

Having probed the thermal sensitivity of coagulation in tumours, we next investigated whether tumour-targeted gold NRs could specify coagulation to occur in tumour tissues. Rod-shaped gold NPs are precisely tunable plasmonic nanomaterials that may be synthesized in bulk, have narrow size distributions and have optical absorption coefficients $10^4–10^6$ times higher than those of conventional organic fluorochromes[19–21]. Previously, we demonstrated that polyethylene glycol-coated gold NRs (PEG–NRs) have >17 h circulation half-lives in mice and can passively target tumours in mice through their fenestrated angiogenic blood vessels to direct precise tumour heating with otherwise benign NIR energy (Supplementary Fig. S2; refs 23–25). Because NIR light can penetrate several centimetres in human tissue, it provides an attractive external input to actuate vascular disruption in tumours[26]. To examine NR-directed coagulation, PEG–NRs (10 mg Au kg^{-1}) or saline were intravenously administered to mice bearing bilateral MDA-MB-435 tumours (Fig. 2c,d). After PEG–NR clearance from circulation (72 h post-injection), fluorescent fibrinogen was intravenously injected and the right flanks of mice were irradiated with NIR light ($\sim$1 W cm^{-2}), generating focal tumour surface temperatures of $\sim$49 °C in PEG–NR-injected mice, while saline-injected tumour surface temperatures remained below $\sim$37 °C (Fig. 2c). At 24 h post-injection, irradiated tumours on NR-injected mice displayed localized accumulation of fibrinogen (Fig. 2d), while tumours with PEG–NRs or NIR energy alone and peripheral tissues lacked this feature. Histopathological analysis revealed that fibrin(ogen) deposition formed a broad interstitial mesh in heated tumours, indicating that NR heating could disrupt tumour blood vessels to activate extravascular coagulation (Supplementary Fig. S2).

We next investigated the potential for a biological signalling module to autonomously survey the host vasculature for angiogenic tumour receptors and, in their presence, engage the extrinsic coagulation cascade. Such a system would operate without the need for any external electromagnetic inputs (for example NIR energy) and could potentially amplify NP targeting to deep-seated and disseminated cancers. We used a truncated, tumour-targeted version of the human protein tissue factor (tTF–RGD), which harnesses an RGD peptide motif to induce coagulation on binding to angiogenic $\alpha_v\beta_3$ receptors[27–31] (Fig. 2e). When tTF is separated from essential cell surface lipid co-factors, its activity towards FX activation diminishes by five orders of magnitude[32]. This nearly digital dependence on cell-surface localization has enabled tumour-targeted tTFs to specifically activate coagulation in mouse cancer models and, recently, in human cancer patients[27,28]. As with PEG–NR signalling modules, we first probed the relative accumulation of fluorescently labelled fibrinogen and albumin in MDA-MB-435 tumours of mice injected with varying doses of tTF–RGD proteins. At 24 h after injection, we observed a macroscopic appearance of haemorrhage in tumours on mice injected with tTF–RGD (>15 µg tTF–RGD/mouse), corresponding to the tumour-specific accumulation of fibrinogen in dendritic, vascular patterns, which were absent from control tumours (Fig. 2f,g, Supplementary Fig. S3). Microscopically, this appearance of vascular coagulation was corroborated by the abundant localization of fibrin(ogen) within tumour blood vessels (Fig. 2g).

Together, we found that both PEG–NR and tTF–RGD signalling modules produced tumour-specific coagulation, highlighting the potential for localized coagulation to communicate the tumour's location to receivers in circulation. We next set out to develop receiving NPs that could efficiently target regions of coagulation
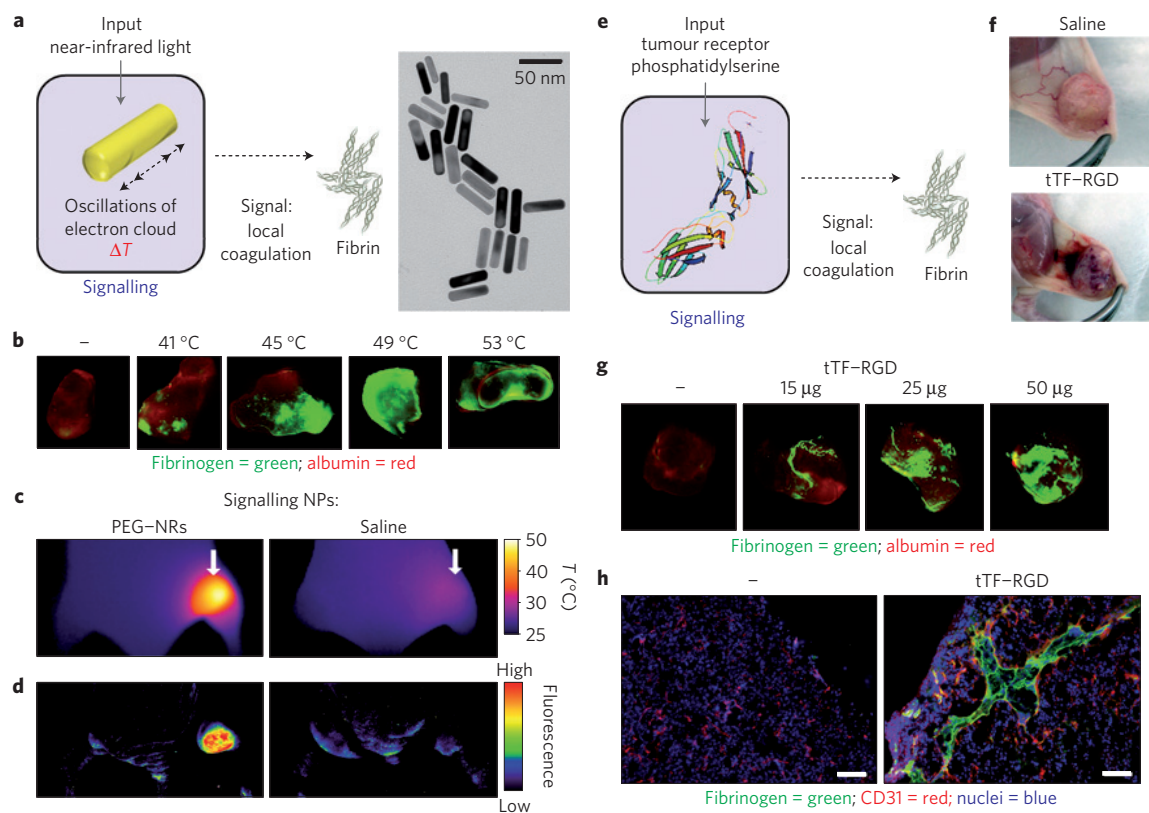
Figure 2 | 'Signalling' component characterization. a, Schematic representation of NR-directed coagulation and transmission electron microscopy of NIR-absorbing NRs. Gold NRs are targeted to tumours to specify local coagulation-cascade activation through photothermal conversion of NIR energy. **b**, Probing the coagulation-dependent and independent protein tropism to heated tumours. Fibrinogen and albumin were labelled with unique NIR fluorochromes and injected into mice bearing bilateral MDA-MB-435 tumours. Immediately following injection, one tumour on each mouse was heated using a temperature-controlled water bath. At 24 h post-injection, mice were dissected and tumours imaged for the relative abundance of fibrinogen (green) and albumin (red). **c**, Thermographic imaging of PEG–NR- and saline-injected mice under NIR irradiation of the right flank. **d**, Fluorescence reflectance imaging of mice to visualize fibrinogen tropism to PEG–NR-heated tumours. **e**, Schematic representation of tumour-targeted tissue factor stimulation of the coagulation cascade in response to tumour receptors. Signalling components are ligand-targeted, truncated human tissue factor proteins (tTF–RGD) proteins that are latent in circulation and autonomously gain coagulation-inducing activity on binding to $\alpha_v\beta_3$ receptors in tumour blood vessels and associating with endothelial cell surface phosphatidylserine. **f**, Intraoperative images at 24 h post tissue factor injection revealing tTF–RGD-mediated haemorrhaging. **g**, Probing the coagulation-dependent and independent protein tropism to tumours on tTF–RGD-injected mice. tTF–RGD signalling components were injected intravenously at varying doses alongside mixtures of fluorescent fibrinogen (green, VT750) and albumin (red, VT680) to monitor tTF–RGD-mediated coagulation in tumours. **h**, Histopathologic analysis of tumour fibrinogen distribution without (left) and with (right) 25 µg tTF–RGD signalling component co-injection (red = CD31 blood-vessel stain; green = injected fibrinogen fluorescence; blue = nuclear stain; scale bars = 100 µm).

to deliver therapeutics or act as imaging agents (Fig. 3a). Initially, magnetofluorescent iron oxide nanoworm imaging agents (NWs; Fig. 3b top) were derivatized with a peptide substrate for the coagulation transglutaminase FXIII (G–N–**Q**–E–Q–V–S–P–L–T–L–L–K–X–C–fluorescein)[33–35] to enable receiver incorporation into regions of active coagulation (Fig. 3b bottom, Supplementary Fig. S4). Having observed that external heating of tumours produced localized coagulation, we used this response in an assay to assess the ability of receivers to target tumour coagulation before integrating them with signalling modules. Mixtures of targeted and untargeted NWs, labelled with unique NIR fluorochromes, were intravenously injected into mice bearing two MDA-MB-435 tumours. Immediately following injection, one tumour was submerged in a temperature-controlled water bath for 20 min and mice were dissected at 24 h for fluorescent organ imaging. We found that the accumulation of FXIII–NW receivers was sharply amplified at 45 °C compared with FXIIIControl–NW-bearing peptides without the essential glutamine for FXIII cross-linking (Fig. 3c,d, Supplementary Fig. S5), enabling nearly an order-of-magnitude increase in tumour targeting compared with unheated

tumours. The specificity of heat-induced targeting to coagulation persisted up to 53 °C, although the magnitude of accumulation decreased (Fig. 3e), probably indicating that higher temperatures accelerated intravascular coagulation and occlusion, diminishing the perfusion required for delivery of receiving NWs into tumours. Histopathologically, FXIII–NWs showed marked extravasation and interstitial spreading in heated tumours compared with controls (Fig. 3d, Supplementary Fig. S5), illustrating the capacity of thermal energy to dismantle tumour vascular barriers and direct abundant interstitial receiver accumulation.

We also explored the feasibility of channelling communications through an alternative molecular pathway in the coagulation cascade. NWs were derivatized with a fibrin-binding peptide (Ac–d–d–d–**G–Y–e–C–hyP–cY–G–L–C–Y–I–Q**–K–fluorescein; Fig. 3b) and tested in a similar assay. Fibrin-binding receiving NWs also exhibited nearly a tenfold amplification of targeting to heated tumours (Fig. 3c, Supplementary Fig. S5), with prominent extravascular accumulation histopathologically (Supplementary Fig. S5).

We next constructed model therapeutic receiving modules to provide amplified drug delivery to regions of tumour
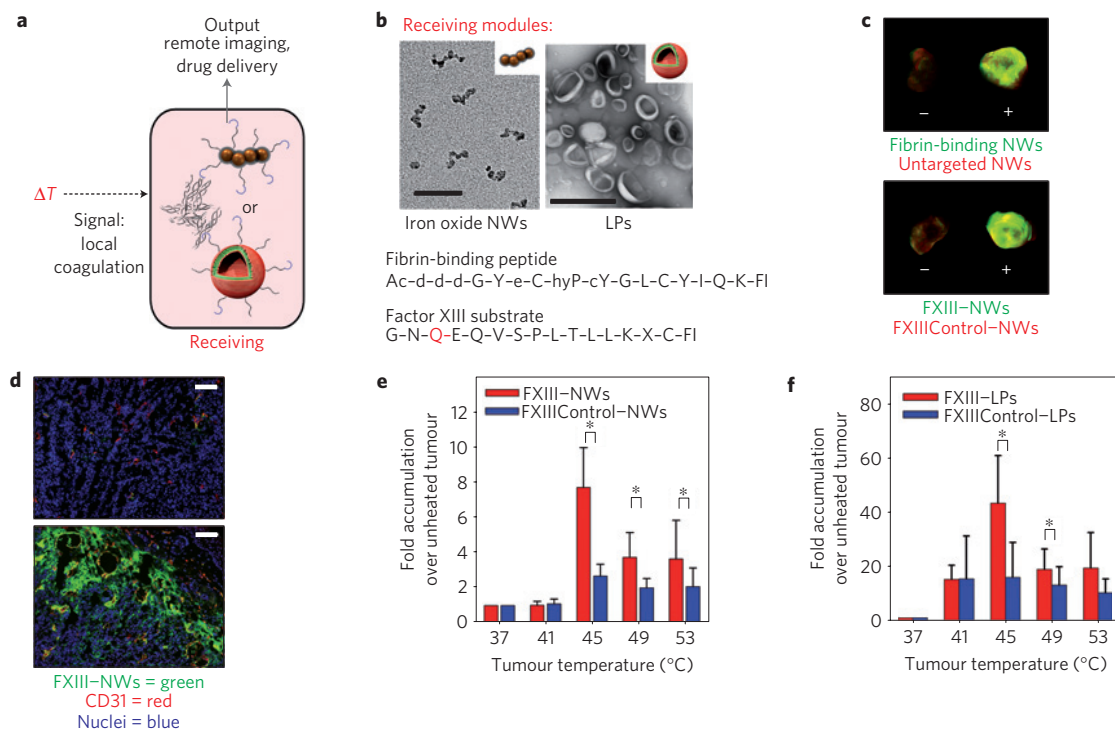
Figure 3 | 'Receiving'-component synthesis and testing. a, Schematic representation of receiving-NP homing to regions of coagulation. NW imaging agents and drug-loaded LPs (top and bottom, respectively) were derivatized with coagulation-targeting peptides to form receiving NPs. **b**, Nanostructure and targeting ligands of receiving NPs. Transmission electron microscopy images of the two classes of nanomaterials used in receiving-NP synthesis: iron oxide NWs (scale bar = 50 nm) and doxorubicin-loaded LPs (scale bar = 400 nm). Two peptides were used to generate receiving NPs: a fibrin-binding peptide and a glutamine-containing substrate for the coagulation transglutaminase FXIII to respectively direct particle binding and covalent attachment in regions of coagulation. **c**, Fluorescence reflectance imaging of receiving-NP homing to externally heated tumours. Mixtures of targeted (green) and untargeted (red) NWs, labelled with the unique NIR fluorochromes VT750 and VT680, respectively, were intravenously injected into mice bearing bilateral MDA-MB-435 tumours. Immediately following injection, one tumour was submerged in a temperature-controlled water bath for 20 min and mice were dissected at 24 h for fluorescent organ imaging. Overlaid fluorescence images are shown for targeted (green) and untargeted (red) receiving-NP accumulation in both heated (+, 45 °C heating) and naive (−) tumours from the same mouse. **d**, Histopathological analysis of receiving-NP homing to heated tumours. Histological sections from naive (top) and heated (bottom, 45 °C) tumours in FXIII–NW-injected mice were stained for CD31 (red) and nuclei (blue) and imaged to reveal receiving-NP distribution (green). (Scale bars = 100 μm.) **e**, Quantifying the amplification of FXIII–NW and FXIIIControl–NW receiver homing to heated over unheated tumours. The fold enhancement of NW targeting is plotted across the range of temperatures tested ($P = 0.02$, 0.03 and 0.04 for the difference between FXIII–NWs and FXIIIControl–NWs at 45 °C, 49 °C and 53 °C, respectively; paired, two-sided t-test, $n = 4$; error bars = s.d.). **f**, Quantifying the amplification of FXIII–LP and FXIIIControl–LP receiver homing to heated over unheated tumours. The fold enhancement of doxorubicin accumulation in tumours is plotted across the range of temperatures tested for FXIII–LPs and FXIIIControl–LPs ($P = 0.025$ and $P = 0.049$ for the difference between FXIII–NWs and FXIIIControl–NWs at 45 °C and 49 °C, respectively; unpaired, two-sided t-test, $n = 3$; error bars = s.d.).

coagulation. Therapeutic receivers were developed by synthesizing doxorubicin-loaded LPs with tethered active (FXIII) or inactive (FXIIIControl) substrates (Supplementary Figs S4, S6). Here, tumour heating to 45 °C directed the accumulation of over 40 times higher doses of doxorubicin in tumours compared with unheated controls and significantly enhanced targeting over inactive FXIIIControl substrate-modified LPs (Fig. 3f).

Having developed signalling and receiving modules and characterized their functions in isolation, we proceeded to study the ability of integrated NP systems to communicate and amplify tumour targeting *in vivo* (Fig. 4a). We began by testing the ability for communication to amplify the targeting of magnetofluorescent FXIII–NW receiving modules to tumours. PEG–NRs (or saline) were intravenously injected into mice bearing bilateral MDA-MB-435 tumours. After NR clearance from circulation (72 h), mixtures of active and inactive receiving NPs (FXIII–NWs and FXIIIControl–NWs) labelled with distinct NIR fluorochromes were co-injected intravenously, followed by NIR irradiation of the entire right flank of the mouse (∼0.75 W cm⁻², 810 nm, 20 min) under infrared thermographic observation. At 96 h, the entire

mouse and then the individual explanted organs were fluorescently imaged (Fig. 4b). Thermographic surveillance of photothermal heating showed focal tumour heating only in NR-injected mice (Fig. 4c) and whole-animal imaging at 96 h revealed pronounced homing of FXIII–NWs to NR-heated tumours, with over an order-of-magnitude increase in accumulation above unirradiated contralateral tumours and tumours on saline-injected mice (Fig. 4d,e, Supplementary Fig. S7). Histologically, integrated NP systems produced intense regions of FXIII–NW fluorescence relative to controls, particularly in tumour boundaries where blood vessels were well perfused (Supplementary Fig. S8). NP systems were found to be effective in xenograft cervical tumour models as well, directing several-fold amplification in homing of targeted receiving NPs over untargeted controls (Supplementary Fig. S9).

We next probed the ability of autonomous communication between tTF–RGD signalling modules and FXIII–NW receiving modules to amplify tumour targeting (Fig. 4f). When co-injected alongside FXIII–NW receivers (Fig. 4g), we find that tTF–RGD signalling modules amplify receiver targeting by several-fold over non-communicating controls and over NWs that are
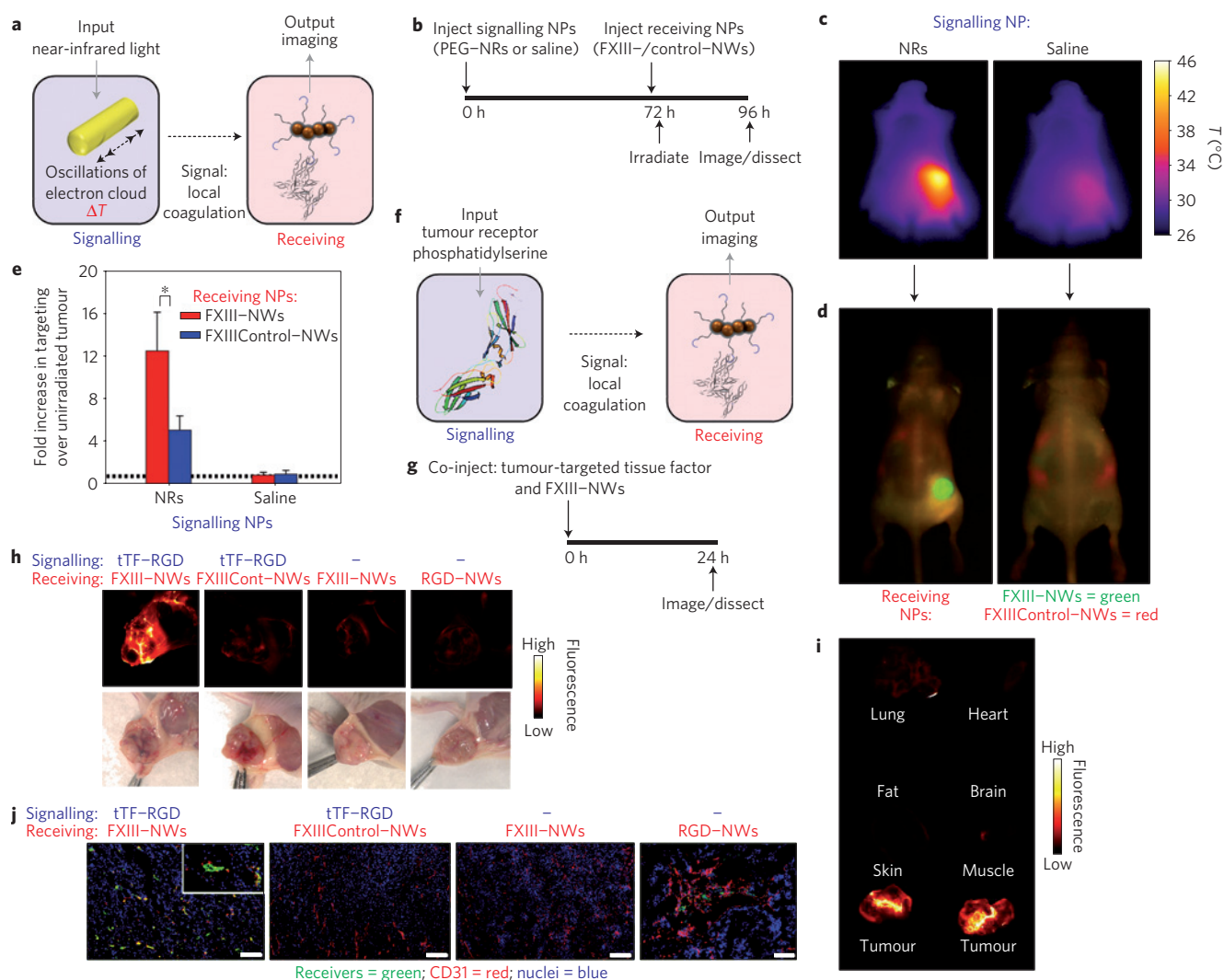
Figure 4 | Amplified tumour targeting with two systems of communicating NPs. a, Schematic representation of communicating NPs. **b**, Experimental timeline for testing communicating NPs. **c**, Thermographic imaging of photothermal PEG–NR heating. At 72 h post NR or saline injection (10 mg Au kg^{-1}), mice were co-injected with coagulation-targeted FXIII–NWs and untargeted FXIIIControl–NWs and their right flanks were broadly irradiated (810 nm, ~0.75 W cm^{-2}, 20 min) under infrared thermographic surveillance to reveal surface temperatures. **d**, Overlaid fluorescence reflectance image of targeted and untargeted receiving-NP homing. At 24 h post-irradiation, whole-animal fluorescence imaging revealed the distributions of coagulation-targeted (FXIII–NWs, green) and untargeted (FXIIIControl–NWs, red) receiving NPs. **e**, Quantification of receiving-NP homing in irradiated versus contralateral unirradiated tumours. After whole-animal imaging, mice were dissected and the fluorescence of each tumour was measured to quantify the homing of receiving NPs. (∗ indicates $P = 0.02$, paired, two-sided t-test; $n = 4$; error bars = s.d.) **f**, Schematic representation of a nanosystem that communicates autonomously in the presence of tumour receptors. **g**, Experimental timeline for testing the autonomous nanosystem in vivo. **h**, Intraoperative imaging of NW receivers. Nu/nu mice bearing a single MDA-MB-435 tumour were intravenously injected with communicating (tTF-RGD + FXIII-NWs) or control (tTF-RGD + FXIIIControl-NWs) systems, FXIII-NWs alone or NWs targeted by the peptide used to direct signalling-component tumour homing (1 mg kg^{-1} tTF-RGD). At 24 h post-injection, tumours were surgically exposed for fluorescent intraoperative imaging of NW homing. (FXIIICont-NWs = FXIIIControl-NWs.) **i**, Tumour specificity of the autonomous nanosystem. Excised organs from mice injected with autonomously communicating nanosystems (tTF-RGD + FXIII-NWs) were imaged for NW fluorescence at 24 h post-injection (1 mg kg^{-1} tTF-RGD). **j**, Histopathological analysis of NW receivers. Histopathological sections from experiments in **h**. At 24 h post-NW injection, mice were killed and tumours were analysed for NW receiver distribution in histology. (Red = CD31 blood-vessel stain, blue = 4,6-diamidino-2-phenylindole nuclear stain, green = NW receiver distribution, RGD-NW scale bar = 100 μm; all others = 200 μm.)

directly targeted by RGD-targeting ligands (Fig. 4h, Supplementary Fig. S10). Similar to the fibrin(ogen) distribution observed during tTF–RGD signalling-module testing, FXIII–NW receivers injected alongside tTF–RGD proteins produced a dendritic pattern of accumulation in tumours, corresponding to abundant intravascular localization immunohistochemically (Fig. 4h–j). This amplified vascular targeting was found to be specific for tumours over normal organs and was absent when the coagulation inhibitor heparin was administered alongside signalling and

receiving modules (Fig. 4i, Supplementary Fig. S10). Further, we found that tTF–NGR signalling modules, which target CD13 angiogenic receptors, were also able to amplify receiver targeting to tumours (Supplementary Fig. S10), highlighting the capacity for autonomously communicating systems to be customized for specific molecular cancer signatures.

As a proof of principle that NP communication could improve tumour drug delivery and therapy, we studied the efficacy of a therapeutic communicating nanosystem (Fig. 5a). We found that
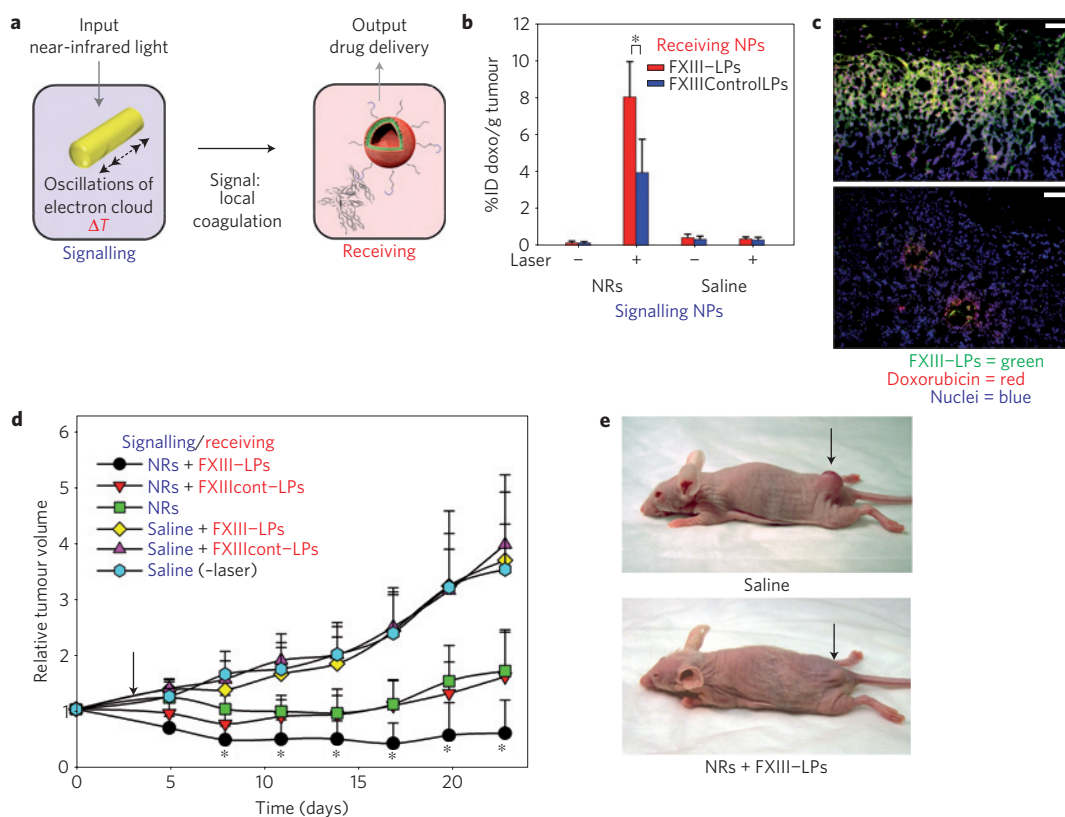
Figure 5 | Amplified tumour therapy with communicating NPs. a, Schematic representation of a therapeutic system of communicating NPs. **b**, Quantification of doxorubicin-loaded LP receiver homing in irradiated versus contralateral unirradiated tumours. At 96 h after signalling NP injection, mice were dissected and the doxorubicin fluorescence of each tumour homogenate in acidic ethanol was measured to quantify the homing of receiving NPs. (∗ indicates $P = 0.021$, unpaired, two-sided t-test, $n = 4$; error bars = s.d.). **c**, Histopathological analysis of NR-directed FXIII–LP targeting and doxorubicin delivery. Histopathological sections from the integrated NP signalling experiments in **b**. At 24 h post NW injection, mice were killed and tumours were analysed for FXIII–LP and doxorubicin distributions in histology. (Red = doxorubicin, blue = 4, 6-diamidino-2-phenylindole nuclear stain, green = FXIII–LP distribution.) (Scale bars = 100 μm.) **d**, Tumour volumes following a single treatment with communicating NP systems and controls. Tumours in all treatment groups except 'Saline (− laser)' were exposed to NIR irradiation for 20 min (∼0.75 W cm^{-2}, ∼810 nm, arrow) 72 h after intravenous NR or saline injection ($P < 0.05$ for NR + FXIII–LPs and all other treatment sets between days 8 and 24; analysis of variance, $n = 7$ mice in each set; error bars = s.d.). **e**, Representative images of mice treated with communicating NPs (NRs + FXIII–LPs, below) compared with untreated controls (Saline, above) (20 d post-treatment).

communication between NR signalling modules and FXIII–LP receivers amplified the accumulation of doxorubicin in tumours by over 40-fold (∼8% ID g^{-1}) as compared with the LPs alone (Fig. 5b) and more than sixfold when compared with an optimized LP formulation that targeted endogenous vascular receptors ($\alpha_v\beta_3$ for high-affinity cyclic-RGD peptide-targeted LPs), illustrating the potential for NP communication to amplify drug delivery over NPs directly targeted to tumour receptors (Supplementary Fig. S11). This amplification of drug delivery probably has at least two components: heat-dependent increases in passive accumulation due to improved extravasation in tumours (as indicated by FXIIIControl–LPs and consistent with previous observations[22]) and specific biochemical recognition of the coagulation process by the peptide coating. Histologically, FXIII–LPs formed a broad interstitial mesh in NR-heated tumours, with released doxorubicin fluorescence emanating from the nuclei of surrounded tumour cells, confirming the delivery and release of active drug within tumour tissues (Fig. 5c).

We finally evaluated the therapeutic efficacy of communicating NPs in mice bearing single MDA-MB-435 human carcinoma tumours. PEG–NRs (10 mg kg^{-1}) or saline were injected into mice and, once NRs had cleared from circulation (72 h), a single intravenous dose of FXIII–LPs, FXIIIControl–LPs or saline (2 mg kg^{-1} doxorubicin) was given, followed immediately by

irradiation with NIR energy (∼0.75 W cm^{-2}, 810 nm, 20 min). We found that a single treatment with communicating NPs directed a prolonged inhibition of tumour growth that was significantly more effective than system components in isolation (FXIII–LPs, FXIIIControl–LPs, NRs) and non-communicating control systems (NRs + FXIIIControl–LPs; Fig. 5d,e; $p < 0.05$ for NR + FXIII–LPs compared with all other treatment groups at each day from 5 to 24 after treatment; one-sided t-test) without detectable weight loss due to systemic toxicity (Supplementary Fig. S11).

Inspired by communication in biological systems, we devised NP systems that communicate to amplify tumour targeting. We demonstrated that systems of synthetic human proteins and simple NPs can be engineered to transmit information through endogenous biological pathways by acting as artificial inputs and outputs to the coagulation cascade. In contrast with 'combination' therapies, where multiple disease pathways in the host are targeted simultaneously, our strategy was composed of components that communicate with one another to more efficiently target regions of disease. We found that communication through the coagulation cascade enhanced the accumulation of receiving modules in tumours by up to 40-fold relative to receiving modules tested in the absence of communication (Supplementary Fig. S12). Further, we found that, after subtracting the baseline targeting of receivers without communication, each NR signalling module in a host tumour

was able to recruit more than 150 FXIII–NWs or more than 35,000 doxorubicin molecules encapsulated within FXIII–LPs (Supplementary Fig. S12), demonstrating the capacity for signal amplification in our approach. Similarly, each tTF–RGD signalling module that accumulated in a host tumour was able to recruit more than ten FXIII–NWs through induction of localized coagulation (Supplementary Fig. S12). The ability for each tumour-receptor-targeted tTF–RGD signalling module in our system to recruit many NP receiving modules contrasts to conventional strategies for ligand-mediated NP targeting, where, depending on NP valency, one or fewer NPs are delivered per ligand-bound receptor in tumours.

We believe that this work motivates a paradigm of 'systems nanotechnology' directed toward the construction of communicative diagnostic and therapeutic agents with sophisticated *in vivo* behaviours. Given the diverse NP and synthetic biological 'building blocks' under development[13–18,36–38], coupled with the plethora of robust biological cascades that could be re-purposed to enable communication between synthetic components, we believe that a wide array of nanosystems could be engineered to more sensitively locate, diagnose and treat a diversity of focal human diseases.

Methods

Signalling-module synthesis. Long-circulating PEG–NRs were synthesized with 5 kDa methoxy PEG–thiol coatings as described previously[23] and tTF–RGD and tTF–NGR signalling modules were expressed in engineered *Escherichia coli*, purified and tested *in vitro* to verify purity (>95%) and activity (factor-X coagulation test) as described in Supplementary Information.

Receiving-module synthesis. Peptide synthesis. The three peptides used in this work were synthesized through 9-fluorenyl-methoxycarbonyl solid-phase peptide synthesis, purified by high-performance liquid chromatography to >90% purity, and characterized through mass spectrometry as described in Supplementary Information.

Iron oxide NW synthesis. Superparamagnetic, dextran-caged iron oxide NWs with a longitudinal size of ~55 nm were synthesized, aminated using 20% v/v ammonium hydroxide, and derivatized with NIR fluorophores as described previously[11]. All peptide-functionalized NWs were characterized through dynamic light scattering and intravenously injected *in vivo* to ensure all targeted NWs and control NWs exhibited similar circulation times. NIR-fluorophore and peptide attachment protocols, along with NW purification methods, are provided in Supplementary Information.

Doxorubicin-loaded LP synthesis. Hydrogenated soy sn-glycero-3-phosphocholine (HSPC), cholesterol and 1,2-distearoyl-sn-glycero-3-phosphoethanolamine-*N*-polyethylene glycol 2000 (DSPE-PEG(2k)) and 1,2-distearoyl-sn-glycero-3-phosphoethanolamine-*N*-[maleimide(polyethylene glycol 2000)] (DSPE-PEG(2k)-MAL) were purchased from Avanti Polar Lipids. Doxorubicin was purchased from Sigma Chemical. Briefly, for targeted LP synthesis, LPs with maleimide groups were prepared from HSPC, cholesterol, DSPE-PEG(2k) and DSPE-PEG(2k)-MAL by lipid film hydration and membrane extrusion. Encapsulation of doxorubicin into the LPs was then carried out using a pH-gradient-driven loading protocol. Free doxorubicin was removed by gel filtration on Sephadex G-50 and the maleimide-terminated LPs were reacted with thiols on peptides (FXIII and FXIIIControl) for 2 h and then purified by gel filtration.

***In vivo* studies.** All studies in mice were approved by the Massachusetts Institute of Technology Committee on Animal Care. MDA-MB-435 human cancer cells were cultured as recommended by the American Type Culture Collection and injected into *nu/nu* mice to establish xenograft tumours as described previously[3,11,23].

Signalling-module distribution and bioactivity *in vivo*. Signalling-module biodistribution and fibrinogen coagulation assays are provided in Supplementary Information.

Immunohistochemical analysis in tumours. For histologic analysis, frozen sections of tumours were prepared. The sections were first fixed with acetone. Rat anti-mouse CD-31 (1:50, BD PharMingen) and biotinylated mouse fibrin(ogen) antiserum (1:50, Nordic) were used for immunochemical staining of tumour tissue sections. The corresponding secondary antibodies were added and incubated for 1 h at room temperature: AlexaFluor-594 goat anti-rat or rabbit IgG (1:1,000; Molecular Probes) and streptavidin Alexa Fluor 594 (1:1,000; Molecular Probes). The slides were washed three times with PBS and mounted in Vectashield Mounting Medium with 4,6-diamidino-2-phenylindole. At least three images from representative microscopic fields were analysed for each tumour sample.

Imaging receiving-NW homing to tumours. Mixtures of NIR-fluorophore-labelled, targeted and control NWs (bearing VT750 and VT680 or VT680 and VT750, respectively) were co-administered intravenously

in PBS (2 mg Fe kg^{-1}) to tumour-bearing *nu/nu* mice to provide an internal control reference for coagulation-specific NW homing. At 24 h post NW injection, mice were killed and organs were analysed for both NIR fluorophores (LI-COR Odyssey Infrared Imaging System). For integrated NP-system characterization, mice were additionally imaged under isofluorane anaesthetic before killing using a whole-animal fluorescence reflectance imaging system (Xenogen, IVIS Imaging System) to visualize the specificity of NW homing to tumours. Images from both organ scanning and whole-animal imaging are displayed throughout the manuscript as overlaid green–red images from both fluorescence channels (VT750 = green and VT680 = red). For autonomously communicating nanosystems, NIR-fluorophore-labelled peptide-bearing NWs (bearing VT750 fluorophores) were intravenously (2 mg Fe kg^{-1}) in PBS to unanaesthetized MDA-MB-435 tumour-bearing *nu/nu* mice alone or alongside various tTF signalling modules (25 μg). At 24 h post NW injection, mice were killed and organs were analysed for NIR-receiver fluorescence (LI-COR Odyssey Infrared Imaging System). For intraoperative fluorescent tumour imaging, mice were anaesthesized and tumours were surgically exposed to reveal detailed tumour fluorescence (LI-COR). For whole-animal organ distribution, tTF–RGD signalling modules were administered intraperitoneally (25 μg) and FXIII–NWs were administered intravenously (2 mg Fe kg^{-1}) to mice bearing a single MDA-MB-435 tumour.

Quantification of receiver homing to tumours. Protocols for fluorescent quantification of NW and doxorubicin quantification are provided in Supplementary Information.

Therapeutic assessment of communicating and control NP systems. Therapeutic studies were conducted by first intravenously administering PEG–NRs or saline into *nu/nu* mice bearing a single MDA-MB-435 tumour. At 72 h post-injection, mice were intravenously administered FXIII–LPs, FXIIIControl–LPs or saline (in a ~150 μl bolus) and broadly irradiated in the vicinity of the tumour with NIR light (810 nm, ~1 W cm^{-2}, 20 min). An additional cohort of mice was administered saline at 0 and 72 h and not exposed to NIR light to isolate any therapeutic efficacy of this input in isolation. At regular intervals after treatment, tumours were measured and mice were weighed. Mice were killed when tumours exceeded 500 mm^3.

References

1. Chan, W. C. & Nie, S. Quantum dot bioconjugates for ultrasensitive nonisotopic detection. *Science* **281**, 2016–2018 (1998).
2. Park, J. H. *et al.* Magnetic iron oxide nanoworms for tumour targeting and imaging. *Adv. Mater.* **20**, 1630–1630 (2008).
3. Xia, Y. N. & Halas, N. J. Shape-controlled synthesis and surface plasmonic properties of metallic nanostructures. *MRS Bull.* **30**, 338–344 (2005).
4. Gref, R. *et al.* Biodegradable long-circulating polymeric nanospheres. *Science* **263**, 1600–1603 (1994).
5. Sengupta, S. *et al.* Temporal targeting of tumour cells and neovasculature with a nanoscale delivery system. *Nature* **436**, 568–572 (2005).
6. Park, J. H., von Maltzahn, G., Ruoslahti, E., Bhatia, S. N. & Sailor, M. J. Micellar hybrid nanoparticles for simultaneous magnetofluorescent imaging and drug delivery. *Angew. Chem. Int. Ed.* **47**, 7284–7288 (2008).
7. Litzinger, D. C. & Huang, L. Phosphatidylethanolamine liposomes—drug delivery, gene-transfer and immunodiagnostic applications. *Biochim. Biophys. Acta* **1113**, 201–227 (1992).
8. Akinc, A. *et al.* A combinatorial library of lipid-like materials for delivery of RNAi therapeutics. *Nature Biotechnol.* **26**, 561–569 (2008).
9. Anderson, D. G., Lynn, D. M. & Langer, R. Semi-automated synthesis and screening of a large library of degradable cationic polymers for gene delivery. *Angew. Chem. Int. Ed.* **42**, 3153–3158 (2003).
10. Leserman, L. D., Barbet, J., Kourilsky, F. & Weinstein, J. N. Targeting to cells of fluorescent liposomes covalently coupled with monoclonal antibody or protein A. *Nature* **288**, 602–604 (1980).
11. Heath, T. D., Fraley, R. T. & Papahdjopoulos, D. Antibody targeting of liposomes: Cell specificity obtained by conjugation of F(ab′)2 to vesicle surface. *Science* **210**, 539–541 (1980).
12. Akerman, M. E., Chan, W. C. W., Laakkonen, P., Bhatia, S. N. & Ruoslahti, E. Nanocrystal targeting *in vivo*. *Proc. Natl Acad. Sci. USA* **99**, 12617–12621 (2002).
13. Hood, J. D. *et al.* Tumour regression by targeted gene delivery to the neovasculature. *Science* **296**, 2404–2407 (2002).
14. Farokhzad, O. C. *et al.* Nanoparticle–aptamer bioconjugates: A new approach for targeting prostate cancer cells. *Cancer Res.* **64**, 7668–7672 (2004).
15. Weissleder, R., Kelly, K., Sun, E. Y., Shtatland, T. & Josephson, L. Cell-specific targeting of nanoparticles by multivalent attachment of small molecules. *Nature Biotechnol.* **23**, 1418–1423 (2005).
16. Geng, Y. *et al.* Shape effects of filaments versus spherical particles in flow and drug delivery. *Nature Nanotech.* **2**, 249–255 (2007).
17. Moghimi, S. M., Hunter, A. C. & Murray, J. C. Long-circulating and target-specific nanoparticles: Theory to practice. *Pharmacol. Rev.* **53**, 283–318 (2001).

551

18. Moghimi, S. M. & Szebeni, J. Stealth liposomes and long circulating nanoparticles: Critical issues in pharmacokinetics, opsonization and protein-binding properties. *Progr. Lipid Res.* **42,** 463–478 (2003).
19. Murphy, C. J. *et al.* Anisotropic metal nanoparticles: Synthesis, assembly, and optical applications. *J. Phys. Chem. B* **109,** 13857–13870 (2005).
20. Jain, P. K., Lee, K. S., El-Sayed, I. H. & El-Sayed, M. A. Calculated absorption and scattering properties of gold nanoparticles of different size, shape, and composition: Applications in biological imaging and biomedicine. *J. Phys. Chem. B* **110,** 7238–7248 (2006).
21. Hu, M. *et al.* Gold nanostructures: Engineering their plasmonic properties for biomedical applications. *Chem. Soc. Rev.* **35,** 1084–1094 (2006).
22. Kong, G., Braun, R. D. & Dewhirst, M. W. Hyperthermia enables tumour-specific nanoparticle delivery: Effect of particle size. *Cancer Res.* **60,** 4440–4445 (2000).
23. von Maltzahn, G. *et al.* Computationally-guided photothermal tumour therapy using long-circulating gold nanorod antennas. *Cancer Res.* **69,** 3892–3900 (2009).
24. Hashizume, H. *et al.* Openings between defective endothelial cells explain tumour vessel leakiness. *Am. J. Pathol.* **156,** 1363–1380 (2000).
25. Maeda, H. The enhanced permeability and retention (EPR) effect in tumour vasculature: The key role of tumour-selective macromolecular drug targeting. *Adv. Enzyme Regul.* **41,** 189–207 (2001).
26. Weissleder, R. A clearer vision for *in vivo* imaging. *Nature Biotechnol.* **19,** 316–317 (2001).
27. Kessler, T. *et al.* Inhibition of tumour growth by RGD peptide-directed delivery of truncated tissue factor to the tumour vasculature. *Clin. Cancer Res.* **11,** 6317–6324 (2005).
28. Bieker, R. *et al.* Infarction of tumour vessels by NGR-peptide directed targeting of tissue factor. Experimental results and first-in-man experience. *Blood* **113,** 5019–5027 (2009).
29. Huang, X. M. *et al.* Tumour infarction in mice by antibody-directed targeting of tissue factor to tumour vasculature. *Science* **275,** 547–550 (1997).
30. El-Sheikh, A., Borgstrom, P., Bhattacharjee, G., Belting, M. & Edgington, T. S. A selective tumour microvasculature thrombogen that targets a novel receptor complex in the tumour angiogenic microenvironment. *Cancer Res.* **65,** 11109–11117 (2005).
31. Persigehl, T. *et al.* Antiangiogenic tumour treatment: Early noninvasive monitoring with USPIO-enhanced MR imaging in mice. *Radiology* **244,** 449–456 (2007).
32. Paborsky, L. R., Caras, I. W., Fisher, K. L. & Gorman, C. M. Lipid association, but not the transmembrane domain, is required for tissue factor activity. Substitution of the transmembrane domain with a phosphatidylinositol anchor. *J. Biol. Chem.* **266,** 21911–21916 (1991).
33. Jaffer, F. A. *et al.* Molecular imaging of factor XIIIa activity in thrombosis using a novel, near-infrared fluorescent contrast agent that covalently links to thrombi. *Circulation* **110,** 170–176 (2004).
34. Tung, C. H. *et al.* Novel factor XIII probes for blood coagulation imaging. *Chembiochem* **4,** 897–899 (2003).
35. Overoye-Chan, K. *et al.* EP-2104R: A fibrin-specific gadolinium-based MRI contrast agent for detection of thrombus. *J. Am. Chem. Soc.* **130,** 6025–6039 (2008).
36. Isaacs, F. J., Dwyer, D. J. & Collins, J. J. RNA synthetic biology. *Nature Biotechnol.* **24,** 545–554 (2006).
37. Hasty, J., McMillen, D. & Collins, J. J. Engineered gene circuits. *Nature* **420,** 224–230 (2002).
38. Jungmann, R., Renner, S. & Simmel, F. C. From DNA nanotechnology to synthetic biology. *HFSP J.* **2,** 99–109 (2008).

Author contributions

G.v.M. and S.N.B. conceived the communication strategy, analysed results and wrote the manuscript; G.v.M., J-H.P., K.Y.L. and N.S. designed and carried out experiments; C.S., R.M., W.E.B., E.R. and M.J.S. contributed reagents and technical expertise.

Additional information

The authors declare no competing financial interests. Supplementary information accompanies this paper on www.nature.com/naturematerials. Reprints and permissions information is available online at http://www.nature.com/reprints. Correspondence and requests for materials should be addressed to S.N.B.

Nanoparticles that Communicate *In Vivo* to Amplify Tumour Targeting

(Supplemental Materials and Methods)

Geoffrey von Maltzahn[1], Ji-Ho Park[2], Kevin Y. Lin[3], Neetu Singh[1], Christian Schwöppe[4], Rolf Mesters[4], Wolfgang E. Berdel[4], Erkki Ruoslahti[5,6], Michael J. Sailor[7,8], Sangeeta N. Bhatia[1,9].

[1]*Harvard-MIT Division of Health Sciences and Technology, Massachusetts Institute of Technology, 77 Massachusetts Avenue, Cambridge, MA 02139 (USA);* [2] *Department of Bio and Brain Engineering, Korea Advanced Institute of Science and Technology, 291 Daehak-ro, Yuseong-gu, Daejeon 305-701, South Korea;* [3] *Department of Chemical Engineering, Massachusetts Institute of Technology, 77 Massachusetts Avenue, Cambridge, MA 02139 (USA);* [4] *Department of Medicine/Hematology and Oncology , University Hospital Muenster, D-48129 Muenster, Germany;* [5]*Vascular Mapping Laboratory, Center for Nanomedicine, Sanford-Burnham Medical Research Institute at UCSB, 3119 Biology II Bldg., University of California, Santa Barbara, CA 93106-9610;* [6]*Cancer Research Center, Sanford-Burnham Medical Research Institute, La Jolla, CA 92037;* [7]*Materials Science and Engineering Program, Department of Chemistry and Biochemistry, University of California, San Diego, 9500 Gilman, La Jolla, CA 92093 (USA);* [8] *Department of Chemistry and Biochemistry, University of California, San Diego, La Jolla, CA 92093-0358;* [9] *Electrical Engineering and Computer Science, MIT, David H. Koch Institute for Integrative Cancer Research, MIT, Department of Medicine, Brigham and Women's Hospital, Howard Hughes Medical Institute.*

Materials and Methods:

PEG-NR Signalling Module Synthesis. PEG-NRs were synthesized as described previously(1). Briefly, highly stable, ~13 nm x 47 nm (Figure 2C) CTAB-coated gold nanorods with longitudinal plasmon resonance at 810 nm (Nanopartz, a division of Concurrent Analytical Inc., Salt Lake City, UT) coated in 250 µM 5 kDa methyl-PEG-thiol (Laysan Bio, U.S., Arab, AL). The solution of 5 kDa methyl-PEG-thiol and

CTAB-coated gold nanorods was gently mixed at room temperature for 1 hr and dialyzed exhaustively against ultrapure water (18 MΩ cm^{-1}) via cellulose ester membrane dialysis (Spectrapor, Rancho Dominguez, CA) to drive PEG addition. Dialyzed samples were filtered through 100 kDa filters (Millipore, Billerica, MA) to remove excess polymer and stored at 4˚C.

tTF-RGD and tTF-NGR Signalling module expression, purification, and in vitro testing

The cDNAs coding for the tTF-containing amino acids 1 - 218 and the respective C - terminal peptide extension were amplified by polymerase chain reaction (PCR) using the primers:

5'-CATGCCATGGGATCAGGCACTACAAATACTGTGGCAGCATATAAT-3'(5'-Primer)

5'-CGGGATCCTATTATGGAGAATCACCTCTTCCTCTGAATTCCCC-3' (3'-Primer) for tTF-RGD and

5'-CGGGATCCTATTATGCATGTGCTCTTCCGTTACCTCTGAATTCCCC-3' (3'-Primer) for tTF-NGR.

With the DNA-Ligation Kit (Novagen, Schwalbach am Taunus, Germany) the cDNA was cloned into the expression vector pET-30(+)a (Novagen) using the BamHI and NcoI sites of the vector. The vectors were introduced in competent *Escherichia coli* cells (BL21 DE3) according to the manufacturer's protocol (Novagen). The bacteria were cultivated in Luria broth medium supplemented with kanamycin (30 µg/ml) at 37°C. When the bacteria cell suspensions reached an OD of ~ 0.6, over-expression of the fusion proteins was initiated by adding 1 mM IPTG (Novagen). After ~16 h, the cells were harvested and 5-7 ml lysis buffer (10 mM Tris-HCl, pH 7.5; 150 mM NaCl; 1 mM MgCl$_2$; 10 µg/ml aprotinin; 20 µl benzonase; 2 mg/ml lysozyme) per gram wet weight were added. The lysed cells were incubated for 90 minutes at room temperature (RT) and centrifuged at 12,000 g for 20 min at 4°C. The pellet was resuspended and homogenized by sonicating in washing buffer (10 mM Tris/HCl, pH 7.5; 1 mM EDTA, 3% Triton X-100). To solibilize the inclusion bodies, 2-4 ml guanidinium buffer (6 M GuCl, 0.5 M NaCl, 20 mM Tris/HCl, pH 7.5; 1 mM DTT) per gram wet weight was added. After incubation overnight at RT, the suspension was centrifuged at 10,000 g for 20 min at 4°C and the supernatant was filtered through a 0.22 µm filter.
The solubilized tTF fusion proteins were refolded and purified by using a multi-step HPLC-based purification process (HPLC unit: ÄKTA purifier 100 System, GE healthcare, Uppsala, Sweden). It consists of an immobilized metal-(copper-)affinity chromatography (IMAC; IMAC Sepharose 6 FF, GE healthcare). The histidine-tagged tTF fusion proteins bind to the immobilized copper ions so that the complete refolding (gradient from 6 M to 0 M urea buffer within 60 min) and washing processes are performed on the column, from which the tTF proteins are eluted by applying 300 mM imidazole. During the subsequent gel filtration the IMAC eluate is conditioned by a buffer exchanging step (20 mM Tris/HCl, pH 8; 20 % glycerol) using Sephadex G-25 (GE healthcare) in order to prepare for the following intermediate anion-exchange chromatography step (AIEX; Q Sepharose HP, GE healthcare; used buffers: 20 mM

Tris/HCl, pH 8; 20 % glycerol +/- 300 mM NaCl). The concluding polishing step again comprises a gel filtration using Sephadex G25 in order to remove any remaining trace impurities and to exchange the puffer to PBS. The final protein solutions (> 95% purity) are stored at -80°C.

Each sample produced was tested for purity (SDS-PAGE, Western Blot, endotoxins, HPLC) and activity (Factor-X coagulation test).

Factor-X activation by tTF Signalling modules
The ability of the tTF proteins to enhance the specific proteolytic activation of Factor (F) X by FVIIa was assessed as described by Ruf et al.(4). Briefly, to each well in a microtiter plate was added 20 µl of: (a) 50 nM recombinant FVIIa (Novo-Nordisc, Bagsværd, Denmark) in TBS-BSA; (b) 0.16 nM - 1.6 µM tTF/tTF-NGR in TBS containing 0.1 % bovine serum albumine (BSA); (c) 25 nM $CaCl_2$ and 500 µM phospholipids (phosphatidylcholine/phosphatidylserine, 70/30, MM; Sigma, München, Germany). After 10 min at RT, 20 µl of the substrate FX (Enzyme Research Laboratories, Swansea, UK) was added in a concentration of 5 µM. Aliquots were removed from the reaction mixture every minute and stopped in 100 nM EDTA. Spectrozyme FXa (American Diagnostica, Greenwich, CT, USA) was added and rates of FXa generation were monitored by the development of color at 405 nm with a microplate reader (Bio-Rad, Hercules, California, USA).

Fibrinogen deposition in heated tumours. Bovine fibrinogen (Sigma) and albumin (Sigma) were reacted with near-infrared fluorochromes (VT750-NHS or VT680-NHS) at a 2:1 fluorophore: protein molar ratio in PBS for ~2 hrs and dialyzed extensively at 4°C against PBS to remove unreacted fluorophores. The product of the dialysis was passed through a 0.1µm filter, quantified using a BCA protein assay (Pierce), and assessed for fluorophore labelling via the absorption at the peak fluorphore absorbance (λ_{max}=750 and 680 nm, respectively, for VT750 and VT680). This reaction generated fibrinogen and albumin protein stocks carrying ~1 fluorophore/protein. To assess whether fibrinogen and albumin home to heated tumours, ~1 nanomole of both proteins (bearing distinct NIR-fluorophores) was injected intravenously into mice bearing bi-lateral MDA-MB-435 carcinoma tumours. Immediately following injection, one tumour on each mouse was externally heated using a temperature-controlled water bath set to between 41-53°C for 20 min. At 24 hrs post-injection, mice were dissected and both tumours fluorescently imaged for the relative abundance of fibrinogen and albumin (LI-COR Odyssey Infrared Imaging System). To ensure that fluorophores did not optically or molecularly skew homing results, all fluorescent experiments were performed with equal numbers of mice allocated to VT750-fibrinogen/VT680-ablumin and VT680-fibrinogen/VT750-albumin administration at each temperature tested. Increases in protein tropism to heated tumours were analyzed by combining the fold increase in targeting observed for both fluorophore orientations (n=4 mice at each temperature tested).

Biodistribution and photothermal heating of passively-targeted nanorod Signalling modules in vivo. Nude mice were injected subcutaneously in the hind flank with ~$2x10^6$ MDA-MB-435 cells. After 2-3 weeks, animals were anaesthetized with isoflurane and injected through the tail vein with PEG-NRs in 0.15 M NaCl, 0.1 M Na Phosphate buffer, pH 7.2 (10 mg Au/kg, ~150ul bolus). Biodistribution was assessed by collecting

organ samples for inductively-coupled plasma mass spectrometry (Thermo-Scientific Finnigan ELEMENT2). Samples were frozen, lyophilized, and dissolved in aqua regia, prepared by adding 100 ul of nitric acid + 300 ul of 37% hydrochloric acid for 72 hrs to dissolve gold particles. Then, samples were brought up into 10 mLs of 9.6 mL 2% HNO_3 and analyzed via ICP-MS against standards. Control saline and organ samples with exogenously added PEG-NRs were utilized to calibrate the linearity of this method. All photothermal heating of NRs was conducted at 72 hrs post administration (a time point after which they had completely cleared circulation) under the guidance of infrared thermography to continually illuminate the surface temperature of irradiated regions (FLIR Thermacam S60). A custom diode laser (RPMC Lasers Inc, 810nm, 30 W) was utilized to broadly irradiate the right flank of tumour-bearing mice at ~0.75 W/cm^2 and ~1 W/cm^2 to maintain desired peak tumour temperatures in NR-injected mice (~46°C for initial fibrinogen-homing experiments and integrated nanoparticle system implementation; 20 min exposure).

Quantifying tTF-RGD accumulation in tumours via fluorescence. Quantification of protein accumulation via fluorescence was based on previously described methods.(6-7) tTF-RGD was reacted with near-infrared fluorochrome, VT750-NHS, at a 3:1 fluorophore:protein molar ratio in PBS for ~2 hrs and dialyzed extensively against PBS to remove unreacted fluorophores. This reaction generated tTF-RGD carrying ~1.3 fluorophore/protein. To assess tTF-RGD accumulation in tumours, 25 ug of tTF-RGD was injected intravenously into unanaesthetized mice bearing bi-lateral MDA-MB-435 carcinoma tumours. At 24 hrs post-injection, mice were euthanized and tumours excised and weighed. Tumours were homogenized with 100 mL of SDS lysis buffer (0.1% SDS, 10 mM Tris, pH 7.6) per 30 mg of tissue, heated to 95°C for 10 minutes, and spun down at 16000 G's for 10 minutes. Supernatant fluorescence was quantified (LI-COR) and compared to a standard curve. Standards were prepared by the same procedure using tumours from uninjected animals and spiking them with known amounts of fluorophore.

Probing tTF Signalling module-mediated tumour coagulation via fibrin(ogen) deposition in tumours. To assess tTF-mediated coagulation in mice, ~1 nanomole of both fibrinogen and albumin proteins (bearing distinct NIR-fluorophores) were injected intravenously alongside varying amounts of tTF, tTF-RGD, or tTF-NGR into unanaesthetized mice bearing a flank MDA-MB-435 carcinoma tumour. At 24 hrs post-injection, mice were dissected and tumours were fluorescently imaged for the relative abundance of fibrinogen and albumin (LI-COR Odyssey Infrared Imaging System). Increases in protein tropism to tumours were analyzed by assessing mean tumour fluorescence (n=4 mice with each type of tTF tested).

Immunohistochemical analysis in tumours. For histologic analysis, frozen sections of tumours were prepared. The sections were first fixed with acetone. Rat anti-mouse CD-31 (1:50, BD PharMingen) and biotinylated mouse fibrin(ogen) antiserum (1:50, Nordic) were used for immunochemical staining of tumour tissue sections. The corresponding secondary antibodies were added and incubated for 1 hour at room temperature: AlexaFluor-594 goat anti-rat or rabbit IgG (1:1,000; Molecular Probes), streptavidin Alexa Fluor 594 (1:1000; Molecular Probes). The slides were washed three times with PBS and mounted in Vectashield Mounting Medium with DAPI. At least

three images from representative microscopic fields were analyzed for each tumour sample.

Peptide Synthesis. The three peptides used in this work: a fibrin-binding peptide (Ac-d-d-d-**G-Y-e-C-hyP-cY-G-L-C-Y-I-Q**-K-(K-Fluorescein)) (binding sequence in bold), a peptide substrate for the transglutaminase Factor XIII (G-N-**Q**-E-Q-V-S-P-L-T-L-L-K-X-C-(K-Fluorescein)) (active glutamine in bold; X=6-aminohexanoic acid linker), and a control substrate for FXIII termed "FXIIIControl" (G-N-**A**-E-Q-V-S-P-L-T-L-L-K-X-C-(K-Fluorescein)) (single amino acid substitution in bold) were synthesized via standard FMOC solid-phase peptide synthesis (MIT Biopolymers Core or Tufts University Core Facility). Products were HPLC-purified to >90% purity and characterized via mass spectrometry. Fibrin-binding peptides were cyclized by bubbling air into 10 µM aqueous peptide solutions overnight, followed by lyophilization for subsequent use.

Receiving Module NP Syntheses. Superparamagnetic, dextran-caged iron oxide nanoworms (NWs) with a longitudinal size of ~55 nm were synthesized, aminated using 20% v/v ammonium hydroxide, and derivatized with near-infrared fluorophores as described previousl (2). Fibrin-binding peptides were attached to NWs via their exogenous lysine by first reacting fluorophore-labelled NWs with the bifunctional linker NHS-PEO$_5$-NHS (Pierce) in phosphate buffered saline pH 7.2 (PBS) at a 5000:1 linker:NW molar ratio to prevent cross-linking. Following activation with linker, NWs were filtered using a gel filtration column (G50 media) and incubated overnight with cyclized fibrin-binding peptides at ~1000:1 peptide:NW ratio with shaking. After ~12 hrs, NWs were purified from extra peptides by repeated filtration on centrifugal membrane filters (100 kDa size cutoff, Centricon, Millipore) and finally dispersed in PBS for spectrophotometric analysis of peptide labelling. Factor XIII-substrates were attached to NWs via their exogenous cysteine similarly, but with the linker NHS-PEO$_{12}$-Maleimide (Pierce) in place of the bifunctional NHS-PEO$_5$-NHS linker. All peptide-functionalized NWs were characterized via dynamic light scattering (DLS) and intravenously injected *in vivo* to ensure all targeted NWs and control NWs exhibited similar circulation times.

Doxorubicin-loaded liposome synthesis. Hydrogenated soy sn-glycero-3-phosphocholine (HSPC), cholesterol, and 1,2-distearoyl-snglycero-3-phosphoethanolamine-N-polyethylene glycol 2000 [DSPE-PEG(2k)], 1,2-Distearoyl-sn-Glycero-3-Phosphoethanolamine-N-[Maleimide(Polyethylene Glycol 2000)] [DSPE-PEG(2k)-MAL] were purchased from Avanti Polar Lipids (Alabaster, AL). Doxorubicin was purchased from Sigma Chemical Co. (St.Louis, MO). For peptide conjugation, liposomes with maleimide groups were prepared from HSPC, cholesterol, DSPE-PEG(2k), and DSPE-PEG(2k)-MAL in the molar ratio of 75:50:3:3 by lipid film hydration and membrane (100 nm) extrusion method(3). Encapsulation of doxorubicin (DOX) into the liposomes was then carried out using the pH gradient-driven loading protocol(4). Free doxorubicin was removed by gel filtration on Sephadex G-50. After doxorubicin loading, the maleimide-terminated liposomes were reacted with thiols on peptides (FXIII and FXIIIControl) for 2 hrs and then purified by by gel filtration on Sephadex G-50. The peptide-conjugated doxorubicin liposomes were stored in PBS at 4 °C before use.

In vitro cytotoxicity: Cytotoxicity assessments were conducted by the MIT Nanomaterials Toxicity Core using Human HeLa cervical cancer cultures (ATTC) in 96-well plates grown to ~70% confluency. Cells were incubated in quadruplicate with various dilutions of either PEG-NR or LP formulations assessed for viability after 24hrs of incubation using the fluorogenic intracellular esterase sensor Calcein acetoxymethylester (Invitrogen).

Imaging Receiving NW homing to tumours. Mixtures of NIR-fluorophore-labelled, targeted and control NWs (bearing VT750 and VT680 or VT680 and VT750, respectively) were co-adminstered intravenously in PBS (2 mg Fe/kg) to tumour-bearing nu/nu mice as described in the manuscript to provide an internal control reference for coagulation-specific NW homing. Because the half-life of targeted and untargeted FXIII-NWs (as well as LPs used in this study) were several hours and the activity of the transglutaminase FXIII has a half-life of <30min following coagulation induction(5), we chose to inject all Receiving NPs at the initiation of heating or alongside tTF Signalling modules to ensure Receivers would be present in circulation during and throughout the onset of coagulation. At 24 hrs post-NW injection, mice were sacrificed and organs were analyzed for both NIR-fluorophores (LI-COR Odyssey Infrared Imaging System). For integrated nanoparticle system characterization, mice were additionally imaged under isofluorane anaesthetic before euthanization using a whole animal fluorescence reflectance imaging system (Xenogen, IVIS Imaging System) to visualize the specificity of NW homing to tumours. Images from both organ scanning and whole animal imaging are displayed as overlaid fluorescent images from both channels (VT750=green and VT680=red). As with fibrinogen/albumin characterization earlier, all experiments were conducted with VT750-labeled targeted particles alongside VT680-labeled control particles and with VT680-labelled targeted particles alongside VT750-labeled control particles to ensure that fluorophore bias did not perturb results. For initial Receiving module characterization, levels of targeted and control NW homing were plotted by comparing the average NW fluorescence in heated tumours versus unheated tumours (n=4 mice at each temperature). For integrated network evaluation, levels were plotted by comparing the average targeted and untargeted NW fluorescence in irradiated tumours versus un-irradiated tumours (n=4 mice for all conditions). For autonomously-communicating nanosystems, NIR-fluorophore-labeled peptide-bearing NWs (bearing VT750 fluorophores) were intravenously (2 mg Fe/kg) in PBS to unanaesthetized MDA-MB-435 tumour-bearing nu/nu mice alone or alongside various tTF Signalling modules (25 μg). At 24 hrs post-NW injection, mice were sacrificed and organs were analyzed for NIR Receiver fluorescence (LI-COR Odyssey Infrared Imaging System). For intraoperative fluorescent tumour imaging, mice were anaesthesized and tumours were surgically exposed to reveal detailed tumour fluorescence (LI-COR). Levels of NW homing to tumours were plotted by comparing the average NW fluorescence in fully-excised tumours (n=4 mice at each condition). For whole animal organ distribution, tTF-RGD Signalling modules were administered intraperitoneally (25 μg) and FXIII-NWs were administered intravenously (2 mg Fe/kg) to unanaesthetized mice bearing an MDA-MB-435 tumour.

Quantifying Receiver NW accumulation in tumours via fluorescence. Quantification of NW accumulation via fluorescence was based on previously described methods. (6-7) MDA-MB-435 xenografts were established in nu/nu mice and administered with FXIII-NW as described in the manuscript. At 24 hrs post-NW administration, mice were euthanized and tumours excised and weighed. Tumours were homogenized with 100 mL of SDS lysis buffer (0.1% SDS, 10 mM Tris, pH 7.6) per 30 mg of tissue, heated to 95°C for 10 minutes, spun down at 16000 G's for 10 minutes, and re-homogenized. Homogenate fluorescence was quantified (LI-COR) and compared to a standard curve. Standards were prepared by the same procedure using tumours from uninjected animals and spiking them with known amounts of fluorophore.

Quantification of doxorubicin in tissues. MDA-MB-435 xenografts were established in nu/nu mice and administered with FXIII-LPs or FXIIIControl- LPs as described in the manuscript. At 24 hrs post-irradiation or external heating, doxorubicin in tissues was fluorescently quantified in organ homogenates. Briefly, organs were removed, weighed, incubated with 500 μl of 70% EtOH, 0.3 N HCl, and homogenized (Tissue Tearor, Biospec Products) to release doxorubicin from tissues. Following homogenization, another 1 ml of 70% EtOH, 0.3 N HCl, was added to samples and they were centrifuged. Supernatants of samples were analyzed for doxorubicin fluorescence using a fluorescence microplate reader (Molecular Devices, SpectraMax GeminiEM) and compared to standard curves.

Therapeutic assessment of communicating and control nanoparticle systems. Therapeutic studies were conducted by first intravenously administering PEG-NRs or saline into nu/nu mice bearing a single MDA-MB-435 tumour. At 72 hrs post-injection, mice were intravenously administered FXIII- LPs, FXIIIControl- LPs, or saline (in ~150 μl bolus) and broadly irradiated in the vicinity of the tumour with NIR light (810 nm, ~1 W/cm^2, 20 min). An additional cohort of mice was administered saline at 0 and 72 hrs and not exposed to NIR light in order to isolate any therapeutic efficacy of this input in isolation. Each therapeutic cohort included 7 mice, except for the unirradiated saline-only control, which had 6 mice. At regular intervals after treatment, tumours were measured and mice were weighed. Mice were sacrificed when tumours exceeded 500 mm^3.

References:

1. von Maltzahn, G. *et al.* Computationally-guided photothermal tumour therapy using long-circulating gold nanorod antennas. *Cancer Research* . 69 (9), 3892, (2009).

2. Park, J.H. *et al.* Magnetic iron oxide nanoworms for tumour targeting and imaging. *Advanced Materials* **20,** 1630-+ (2008).3. M. J. Hope, M. B. Bally, G. Webb, P. R. Cullis, *Biochimica Et Biophysica Acta* **812**, 55 (1985).

3. L. D. Mayer, M. B. Bally, M. J. Hope, P. R. Cullis, *Biochimica Et Biophysica Acta* **816**, 294 (1985).

4. Ruf,W. et al. Phospholipid-independent and -dependent interactions required for tissue factor receptor and cofactor function. *J Biol Chem*. **266**, 2158-2166 (1991).

5. Robinson BR *et al*. Catalytic life of activated factor XIII in thrombi. Implications for fibrinolytic resistance and thrombus aging. Circulation. 2000 Sep 5;102(10):1151-7.

6. Olson, E. S. *et al.* In vivo characterization of activatable cell penetrating peptides for targeting protease activity in cancer. *Integrative Biology* **1**, 382-393 (2009).

7. Aguilera, T. A., Olson, E. S., Timmers, M. M., Jiang, T. & Tsien, R. Y. Systemic in vivo distribution of activatable cell penetrating peptides is superior to that of cell penetrating peptides. *Integrative Biology* **1**, 371-381 (2009).
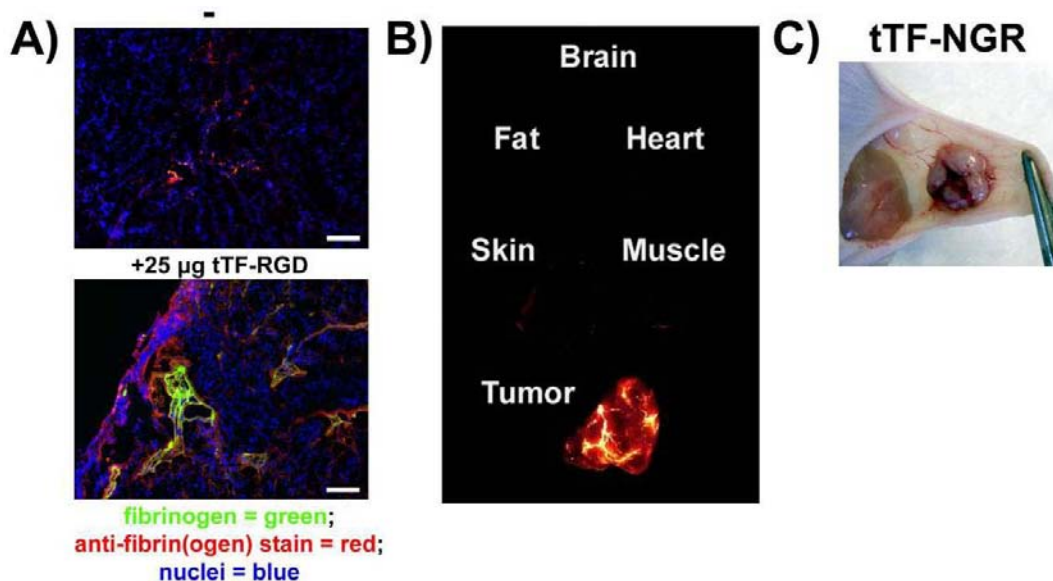
Supplemental Figures:
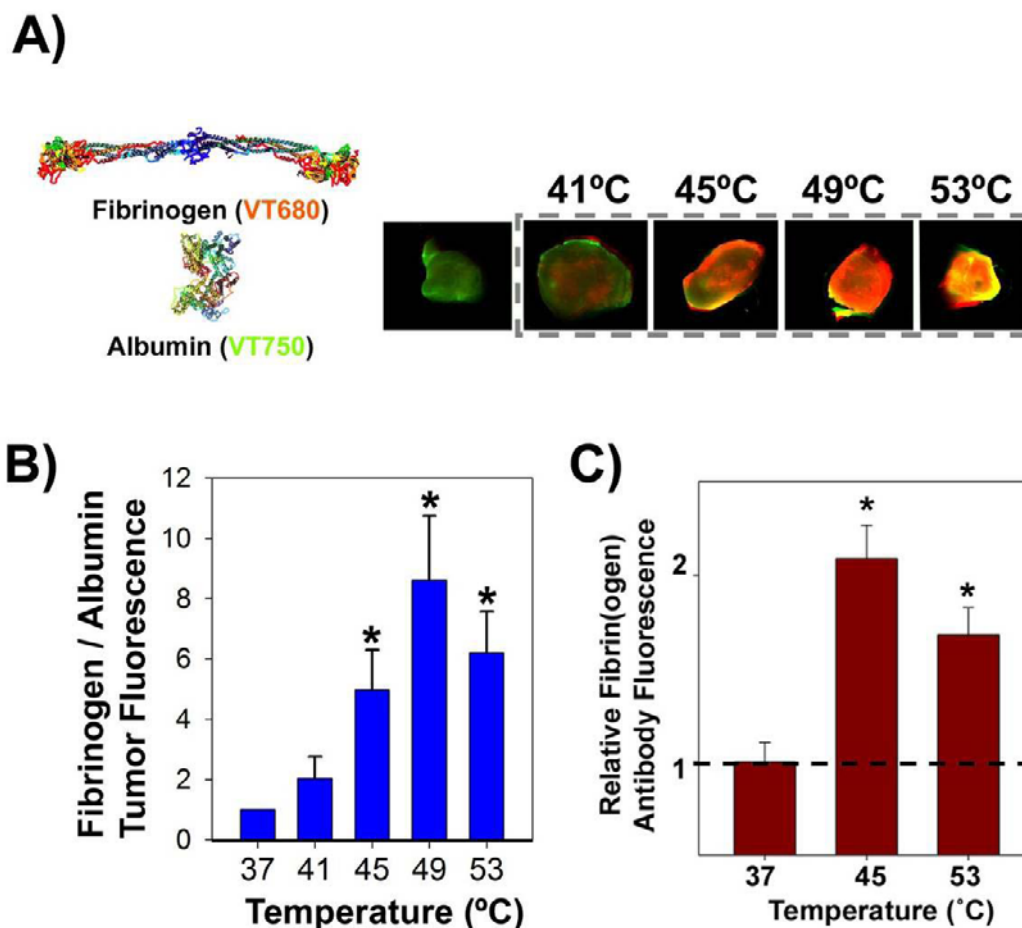
Figure S1. *Specific fibrinogen tropism to heated tumours.* A) *Probing the coagulation-dependent and –independent protein tropism to heated tumours.* Fibrinogen and albumin were labelled with unique near-infrared fluorochromes in the *opposite* channels as in Figure **2A** (VT680 and VT750, respectively) and injected in mice under identical conditions. Reversing the fluorophore labelling on fibrinogen and albumin enables quantitation of protein tropism to heated tumours independent of any potential optical or molecular fluorophore bias. At 24 hrs post-injection, mice were dissected and both tumours imaged for the relative abundance of fibrinogen (red) and albumin (green). Both heated (+ row) and unheated (- row) tumours are displayed across the temperatures tested. **B)** *Quantitation of fibrinogen:albumin fluorescence ratio across tested tumour temperatures.* Data taken under conditions of **2B** and **S1A** were utilized to quantify the relative abundance of fibrinogen and albumin in heated tumours vs unheated. At 45-53˚C, fibrinogen abundance in tumours was significantly enhanced over albumin ($p < 0.05$; 1-sided t-test; 4-mice per temperature). **C)** *Quantitation of anti-fibrin(ogen) binding to sections from unheated and externally-heated tumours.* As an independent measure of fibrin(ogen) deposition in heated tumours, uninjected mice bearing bilateral

MDA-MB-435 tumours had one tumour immersed in a temperature-controlled water bath for 20 minutes and were sacrificed 24 hrs later for histological sectioning. Fluorescent quantification showed significantly enhanced abundance of antibody binding at both 45 and 53°C ($p<0.0001$, 1-sided t-test, 6 separate regions analyzed in each condition).
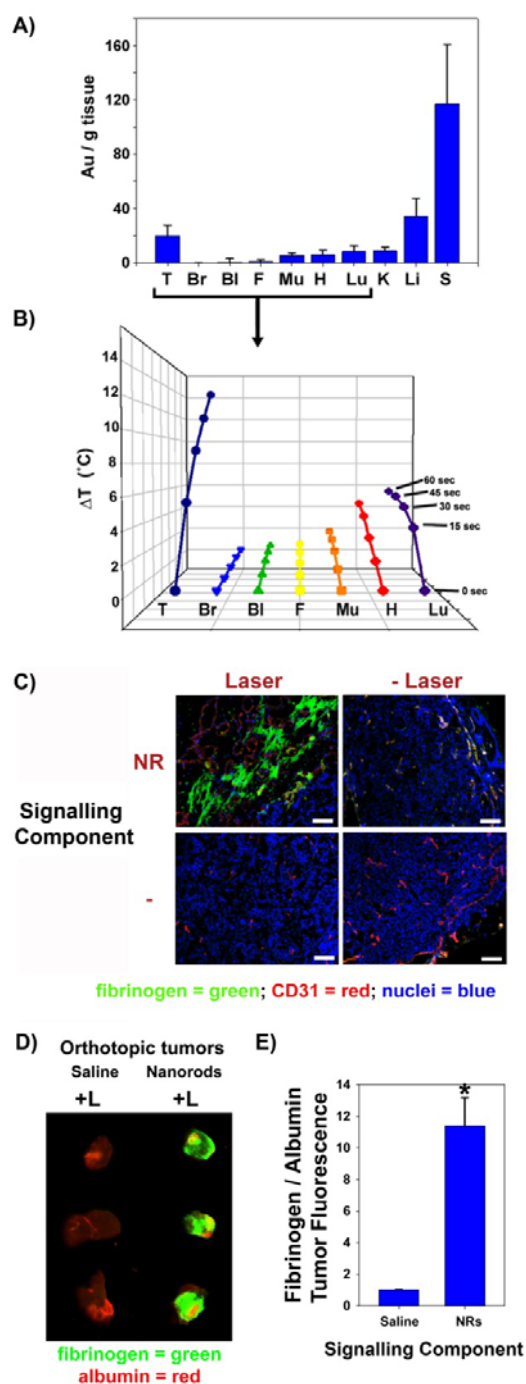
Figure S2. *Nanorod-directed fibrin(ogen) deposition in vivo.* **A)** *PEG-nanorod biodistribution and targeting to MDA-MB-435 tumours 72hrs following intravenous administration, quantified via inductively-coupled plasma mass spectrometry* (3 mice). Y-axis is micrograms Au per gram tissue. (T=tumour, Br=brain, Bl=bladder, F=fat, Mu=muscle, H=heart, Lu=lung, K=kidney, Li=liver, Sp=spleen) **B)** *Ex-vivo heating rates of dissected organs under identical irradiation conditions revealed that NR targeting confers specificity to photothermal tumour heating.* Mice bearing a single

MDA-MB-435 tumour were injected with PEG-NR Signalling modules and, 72 hrs after injection, were dissected for comparison of photothermal organ heating rates. **C)** *Histopathological analysis of NR-directed fibrinogen deposition in tumours.* Mice bearing bilateral MDA-MB-435 tumours were injected with PEG-NRs (10 mg Au/kg) or saline and, 72 hrs later, injected with fluorescently-labeled fibrinogen (VT750) and broadly irradiated on their right side (~1 W/cm^2, 810 nm, 20 min). At 24 hrs post-injection, mice were sacrificed and tumours isolated for histological analysis of fibrinogen distribution (Red=CD31 antibody stain, Blue= DAPI nuclear stain, Green=fibrinogen distribution) (Scale bars=100 μm). **D)** *Probing the photothermal induction of coagulation in orthotopic MDA-MB-435 tumours implanted deep in the mammary fat pad.* Mice bearing a single MDA-MB-435 tumour were injected with PEG-NRs (10 mg Au/kg) or saline and, 72 hrs later, injected with fluorescently-labeled fibrinogen (VT750) and albumin (VT680) and broadly irradiated with extracorporeal light (~1.5 W/cm^2, 810 nm, 20 min). At 24 hrs post-injection, mice were sacrificed and tumours isolated for fluorescent imaging of relative fibrin(ogen) (*green*) and albumin *(red)* accumulation. **E)** *Quantitation of fibrinogen:albumin fluorescence ratio across tested tumour temperatures.* Data taken under conditions of **D)** were utilized to quantify the relative abundance of fibrinogen and albumin in tumours from mice injected with saline and NRs.

A) +25 μg tTF-RGD

fibrinogen = green;
anti-fibrin(ogen) stain = red;
nuclei = blue

B) Brain / Fat / Heart / Skin / Muscle / Tumor

C) tTF-NGR

Figure S3. *tTF-RGD and tTF-NGR Signalling module characterization* **A)** *Anti-fibrin(ogen) antibody stain reveals little fibrin(ogen) in tumours of mice injected with saline (*top*) and fluorescent fibrin(ogen) and abundant fibrin(ogen) in tumours of tTF-RGD-injected mice that co-localizes with injected fibrin(ogen) fluorescence* (bottom)(Red = Anti-fibrinogen stain; Green = injected fibrinogen fluorescence; Blue = nuclear stain), top = VT750-labeled fibrinogen without tTF-RGD injection; bottom = VT750-labeled fibrinogen with tTF-RGD injection (1 mg tTF-RGD/kg) (Scale bars = 100 μm). **B)** *Macroscopic distribution of fluorescent fibrinogen in tTF-RGD Signalling module –injected mice.* Organs were imaged at 24 hrs following intravenous co-injection of fluorescent fibrinogen with tTF-RGD Signalling module (1 mg tTF-RGD/kg) (~1 nmole fibrinogen; VT750 fluorophore). *Intraoperative images at 24-hrs post-tTF-NGR Signalling module (which binds CD13/aminopeptidase N receptors associated with tumour angiogenesis) injection highlighting modularity of tTF Signalling modules. Nu/nu* mice bearing a single MDA-MB-435 tumour were intravenously injected with tTF-NGR (1 mg of tTF-NGR/kg) and dissected 24 hrs later. Administration of both tTF-NGR or tTF-RGD led to the macroscopic appearance of tumoural hemorrhage and RBC stasis, while saline-injected mice harbored ivory-hued tumours (see Figure 2 of manuscript for tTF-RGD and saline).
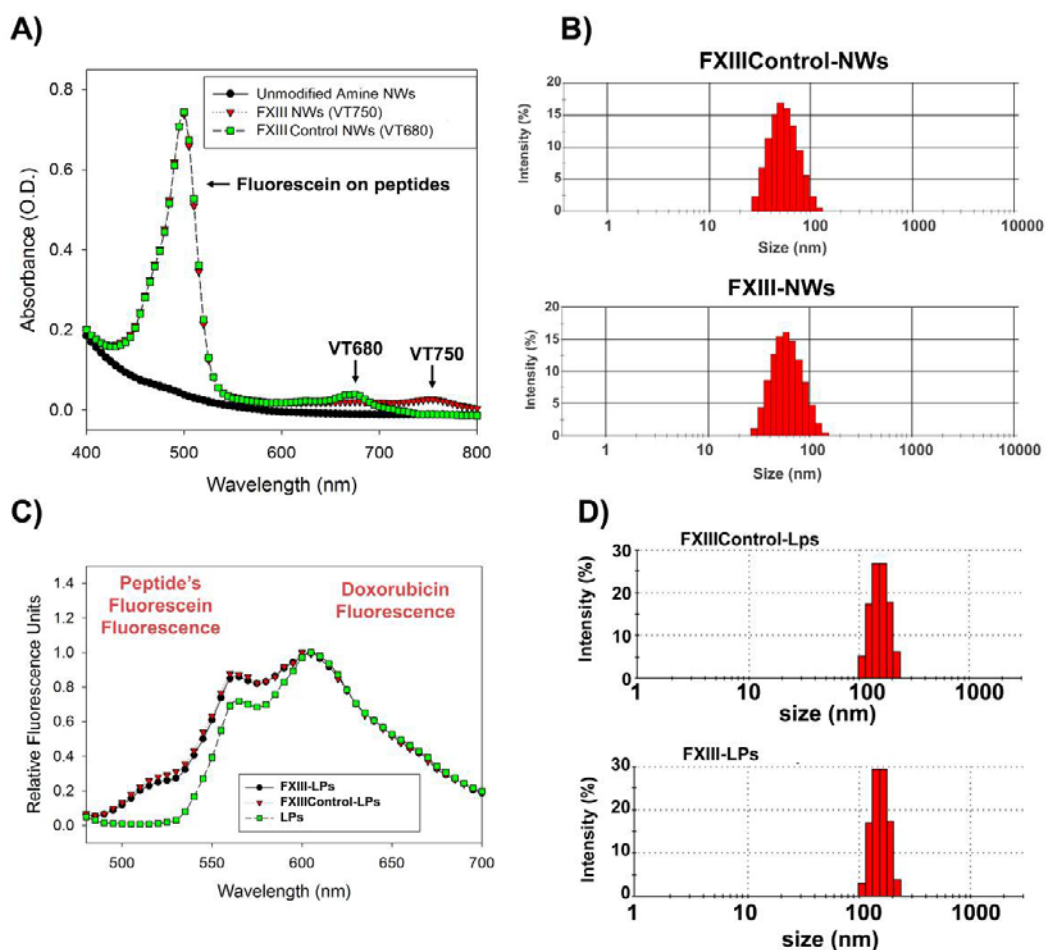
Figure S4. *Spectrophotometric, fluorescent, and size characterization of Receiving modules.* **A)** Spectrophotometric characterization of NW Receiving module functionalization. Aminated NWs were conjugated with NHS-activated NIR fluorochromes (VT680 or VT750) to allow fluorescent imaging and subsequently linked to thiol-containing FXIII-substrate peptides or FXIIIControl-peptides. The spectra NWs were utilized to quantify the number of peptides and NIR-fluorochromes per particle (~600 FXIII- or FXIIIControl-peptides/NW and ~12-15 fluorochromes/NW, respectively). Conjugation conditions were optimized to produce populations with approximately equal numbers of peptides in the FXIII-NWs and FXIIIControl-NWs. **B)** Dynamic light scattering characterization of FXIIIControl-NW and FXIII-NW Receiving modules. After peptide functionalization with NIR-fluorochromes and peptides, samples were analyzed via DLS to probe the hydrodynamic size of each conjugate. **C)** Fluorescent characterization of FXIIIControl-LPs and FXIII-LPs. The fluorescence emission spectra of Fluorescein-conataining FXIII- and FXIIIControl-peptides was utilized to ensure similar surface density on LP conjugates (excitation: 444 nm; cutoff: 455 nm; emission 480 nm-700 nm). **D)** Dynamic light scattering characterization of FXIII-LP and FXIIIControl-LP Receiving modules. After peptide functionalization, LP Receiving modules were analyzed via DLS to probe the hydrodynamic size of each conjugate.
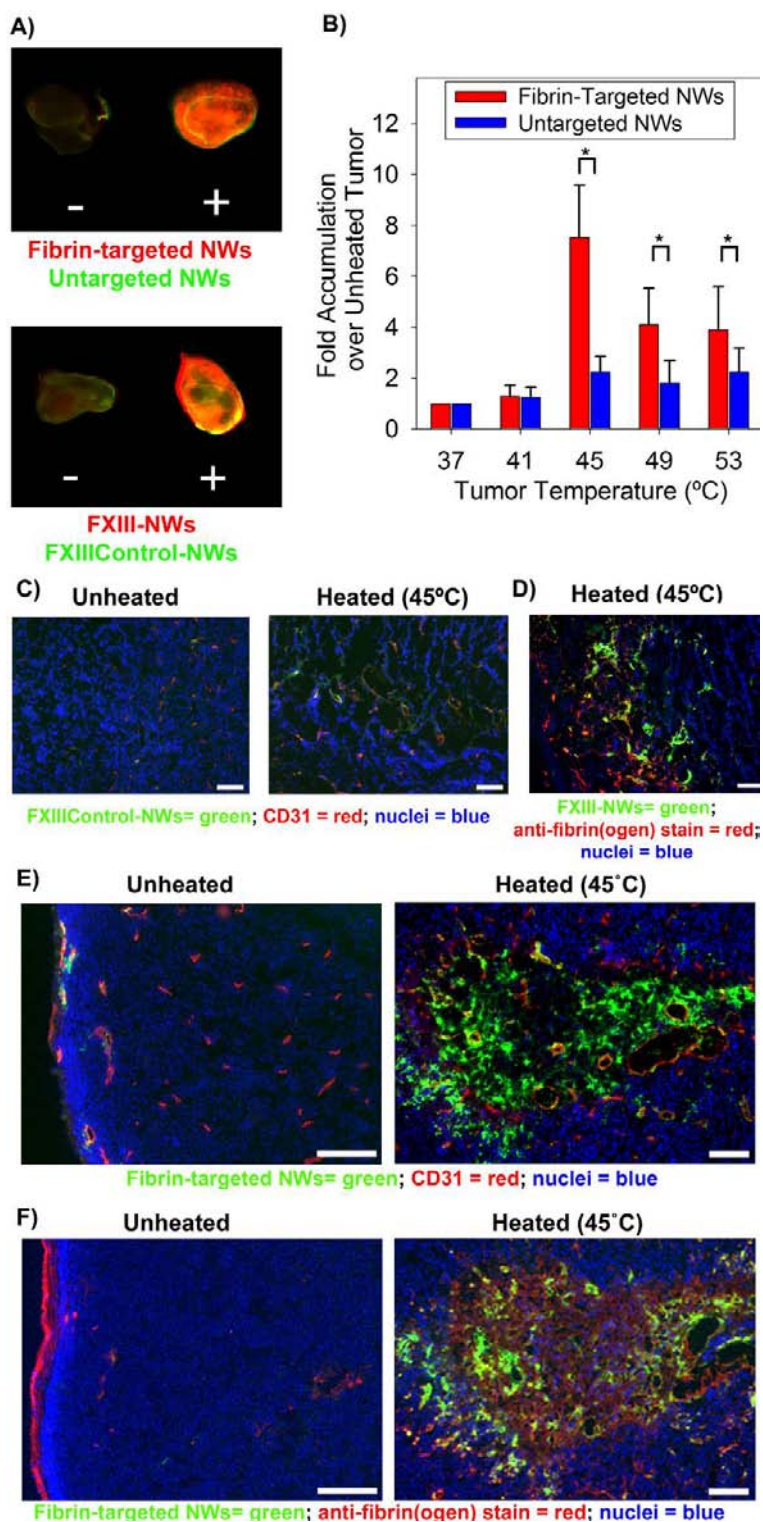
Figure S5. *NW Receiver Characterization.* **A)** *Fluoresence reflectance imaging of Receiving module homing to externally-heated tumours.* Mixtures of targeted (red) and untargeted (green) NWs (labelled with the opposite orientation of NIR-fluorochromes

used in Figure **3C** to control against potential optical or molecular fluorochrome bias to Receiving module detection in heated vs unheated tumours**)** VT680 and VT750, respectively, were intravenously injected into mice bearing bilateral MDA-MB-435 tumours. Immediately following injection, one tumour was submerged in a temperature-controlled water bath for 20 min and mice were dissected at 24 hrs for fluorescent organ imaging. Overlaid fluorescence images are shown for targeted (green) and untargeted (red) Receiving module accumulation in both heated ("+", 45ºC heating) and naïve ("-") tumours are shown from the same mouse. **B)** *Fluorescent quantification of fibrin-binding and untargeted-NW Receiving module homing to heated over unheated tumours.* The fold enhancement of NW targeting is plotted across the range of temperatures tested (n=4 mice in each set, p<0.05 for the difference between fibrin-binding-NWs and untargeted-NWs at 45ºC, 49ºC, and 53ºC, respectively). **C)** *Histopathological analysis of FXIIIControl- NWs.* Mice bearing bilateral MDA-MB-435 tumours were injected with control-substrate NWs and one tumour was heated to 45ºC for 20 min. At 24 hrs post-injection, mice were sacrificed and tumours were analyzed for NW distribution in histology using the same exposure conditions for NW imaging as Figure S8, S10, and Figure 3D. (Red=CD31 antibody stain, Blue= DAPI nuclear stain, Green=FXIIIControl- NW distribution) (Scale bar=100 μm) **D)** *Histopathological analysis of FXIII-substrate localization to areas of anti-fibrin(ogen) staining.* Mice bearing bilateral MDA-MB-435 tumours were injected with FXIII-NWs and one tumour was heated to 45ºC for 20 min. At 24 hrs post-injection, mice were sacrificed and tumours were analyzed for NW distribution in histology using the same exposure conditions for NW imaging as Figure S8, S9, and Figure 3D. (Red=anti-fibrin(ogen) antibody stain, Blue= DAPI nuclear stain, Green=FXIII- NW distribution) (Scale bar=100 μm) **E)** *Histopathological analysis of FXIII-substrate localization to areas of anti-fibrin(ogen) staining.* Mice bearing bilateral MDA-MB-435 tumours were injected with FXIII-NWs and one tumour was heated to 45ºC for 20 min. At 24 hrs post-injection, mice were sacrificed and tumours were analyzed for NW distribution in histology using the same exposure conditions for NW imaging as Figure S8, S9, and Figure 3D. (Red=anti-fibrin(ogen) antibody stain, Blue= DAPI nuclear stain, Green=FXIII- NW distribution) (Scale bar=100 μm) **F)** *Distribution of fibrin-targeted NWs in unheated tumours.* (Red=CD31 antibody stain, Blue= DAPI nuclear stain, Green=fibrin-targeted NW distribution) (Scale bar=100 μm) **G)** *Distribution of fibrin-targeted NWs in unheated tumours.* (Red=CD31 antibody stain, Blue= DAPI nuclear stain, Green=fibrin-targeted NW distribution) (Scale bar=100 μm) **H)** *Co-localization of fibrin-targeted NWs with anti-fibrin(ogen) antibody staining in heated tumours.* (Red=anti-fibrinogen antibody stain, Blue= DAPI nuclear stain, Green=fibrin-targeted NW distribution) (Scale bar=100 μm) **I)** *Co-localization of fibrin-targeted NWs with anti-fibrin(ogen) antibody staining in heated tumours.* (Red=anti-fibrinogen antibody stain, Blue= DAPI nuclear stain, Green=fibrin-targeted NW distribution) (Scale bar=100 μm)
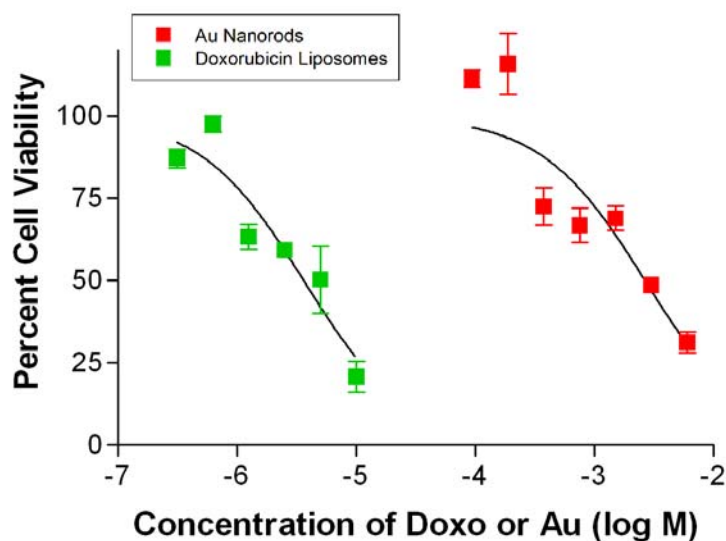
Figure S6. *Cytotoxicity experiments to assess intrinsic toxicity of Au nanorods and doxorobicin-loaded liposomes.* Cytotoxicity assessments were conducted using Human HeLa cervical cancer cultures (ATTC) in 96well plates grown to ~70% confluency. Cells were incubated with various dilutions of either PEG-NR or LP formulations assessed for viability after 24hrs of incubation using the fluorogenic intracellular esterase sensor Calcein acetoxymethylester (each point represents the average of 4 wells in a 96-well plate).
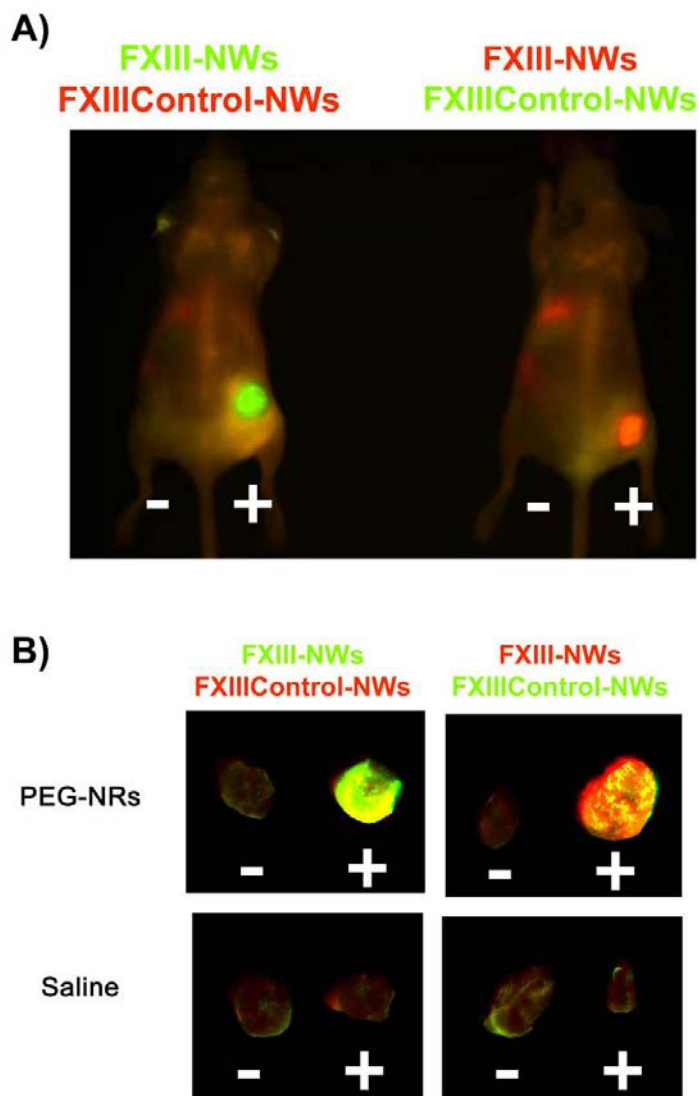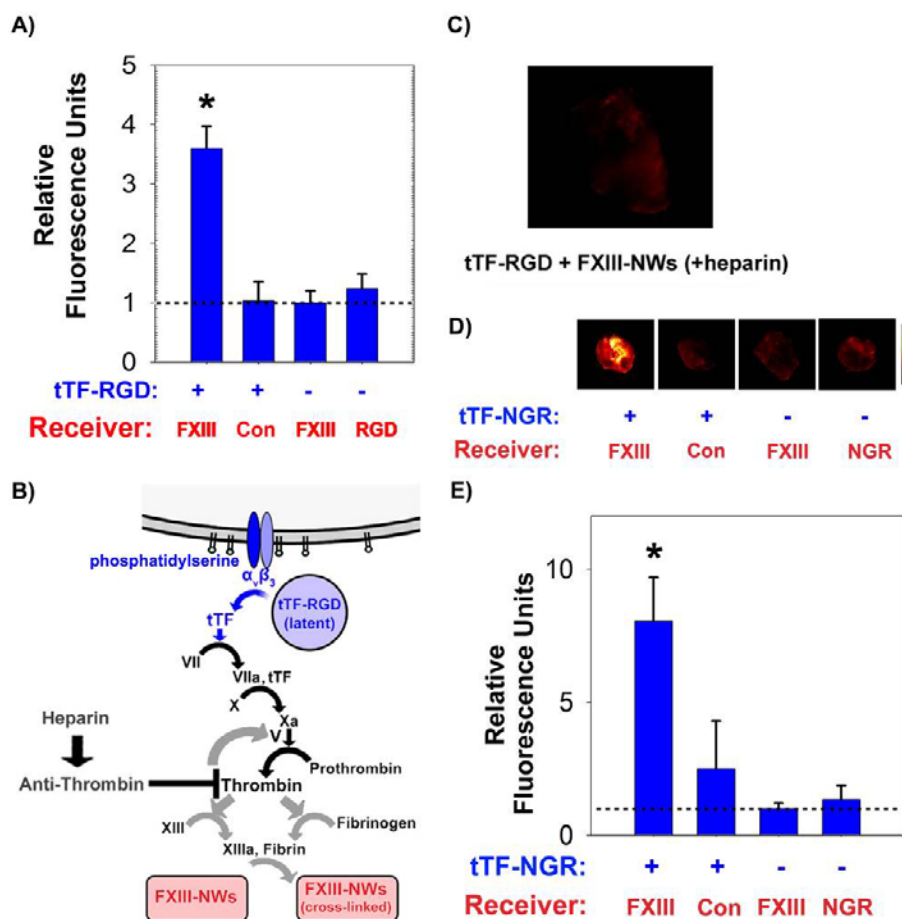
Figure S7. *Integrated communicating nanoparticles from Figure 4D, but with inverted fluorophore-targeting ligand relationships to control against bias and ex-vivo imaging of excised tumours.* A) Simultaneous near-infrared imaging of co-injected: VT750-labeled, FXIII- NWs (green, left mouse) and VT680-labeled, FXIIIControl- NWs (red, left mouse); or VT680-labeled, FXIII-NW (red, right mouse) and VT750-labeled, FXIIIControl- NWs (green, right mouse). Inversion of fluorochrome-NW relationships prevents optical or molecular bias from fluorophores in homing visualization. + indicates broad laser irradiation (810 nm, 0.75 W/cm^2, 20 min). B) Imaging of NW homing in excised tumours from experiments in Figures 4D and S12A. Each box was imaged using the same acquisition parameters for both VT750 (green) and VT680 (red) and contains the left and right tumours from MDA-MB-435-bearing mice.
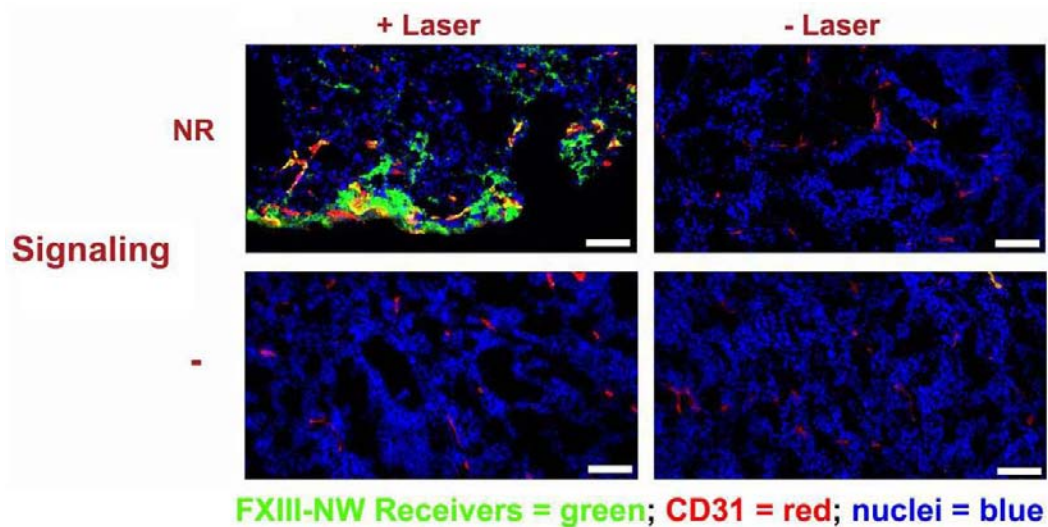
Figure S8. *Histopathological analysis of FXIII-NWs with integrated and disconnected NP communication systems.* Histopathological sections from the integrated NP Signalling experiments in Figures 4C, 4D, 4E and S12. At 24 hrs post-NW injection, mice were sacrificed and tumours were analyzed for FXIII-NW distribution in histology. (Red=CD31 antibody stain, Blue= DAPI nuclear stain, Green=FXIII-NW distribution). (Scale bars = 100 μm)
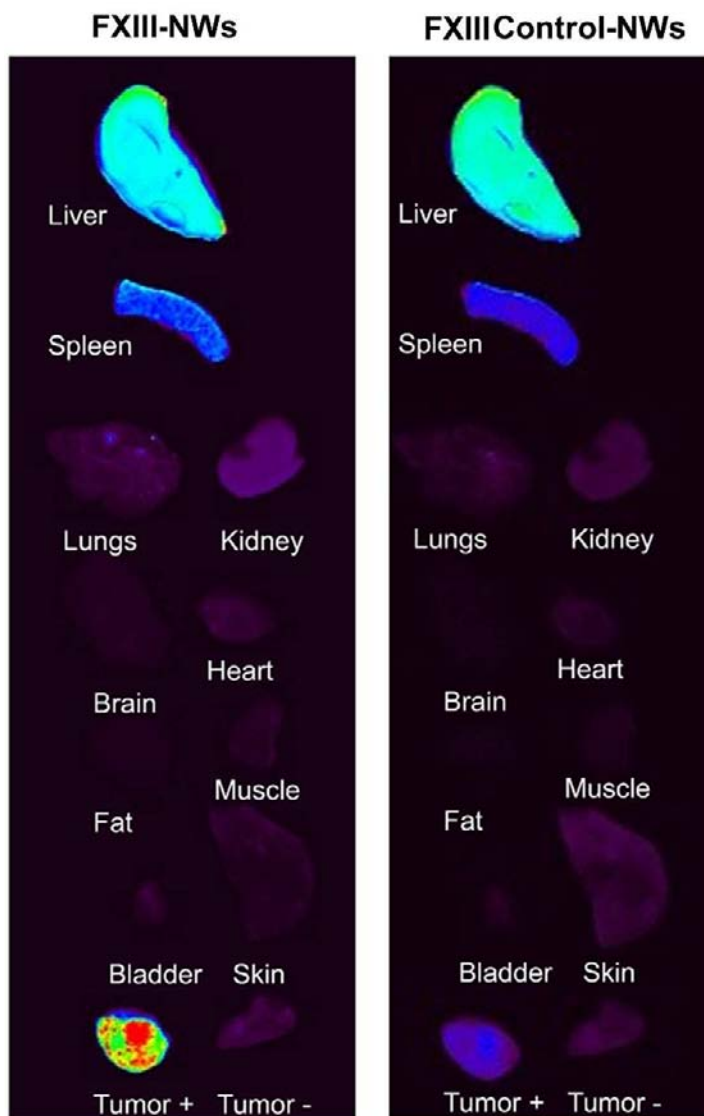
Figure S9. *Function of NP communication to human cervical xenograft tumours.* Athymic (*nu/nu*) mice bearing bilateral Hela human cervical cancer tumours were injected with PEG-NRs and, 72 hrs later, a mixture of FXIII- NWs and FXIIIControl-NWs, labelled with unique NIR-fluorophores, as described for MDA-MB-435 tumour-bearing mice in Figure 4. Immediately following injection of NW mixtures, the right flanks of mice were broadly irradiated with a diode laser source. At 24 hrs post-injection, the homing of FXIII-NWs and FXIIIControl-NWs was visualized using NIR fluorescent organ imaging. ("Tumour +" indicates the irradiated tumour; "Tumour –" was not exposed to diode irradiation)

Figure S10. *Characterization of autonomously-communicating nanosystems.* **A)** *Fluorescent quantitation of NW homing in integrated Signalling networks and controls from mice in experiment from Figure 4H* (Con=FXIIIControl-NWs) (*$p<0.05$ versus all other sets, n=4 mice for each set) **B)** *Heparin-mediated disruption of Signalling network communication.* Schematic of heparin's disruption of communication in hybrid Signalling ne tworks. **C)** *Nu/nu* mice bearing a single MDA-MB-435 tumour were intravenously injected with integrated Signalling networks (tTF-RGD + FXIII-NWs; 1 mg/kg tTF-RGD; 1.5 mg Fe/kg) alongside heparin to prohibit thrombin activation (intravenous bolus of 800 units/kg + intraperitoneal bolus of 500 units/kg 30 minutes later). At 24 hrs post-injection, mice were sacrificed and tumours were surgically removed for fluorescent imaging of NW localization to tumours. Tumours on heparin-injected mice lack characteristic vascular pattern of communication between tTF Signalling modules and FXIII-NW Receivers. **D)** *Modularity of autonomously-communicating nanosystems.* tTF-NGR Signalling modules (which bind CD13/aminopeptidase N receptors associated with tumour angiogenesis) were substituted for tTF-RGD Signalling modules to explore the composability of autonomously-communicating systems. *Nu/nu* mice bearing a single MDA-MB-435 tumour were intravenously injected with communicating (tTF-NGR + FXIII-NWs) or control (tTF-NGR + FXIIIControl-NWs) nanosystems, FXIII-NWs alone, or NWs

targeted by the peptide used to direct tTF-NGR Signalling module tumour homing (1 mg/kg tTF-NGR; 1.5 mg Fe/kg). At 24 hrs post-injection, mice were sacrificed and tumours were surgically removed for fluorescent imaging of NW localization to tumours (Con=FXIIIControl-NWs). **E)** Quantification of average fluorescence from tumour cohorts above (n = 3 or 4 mice in each set; error bar indicates standard deviation of data; Student's one-tailed t-test: p=0.006, 0.0015, and 0.001 for tTF-NGR + FXIII-NWs vs. tTF-NGR + FXIIIControl-NWs, FXIII-NWs, and NGR-NWs respectively) (Con=FXIIIControl-NWs).
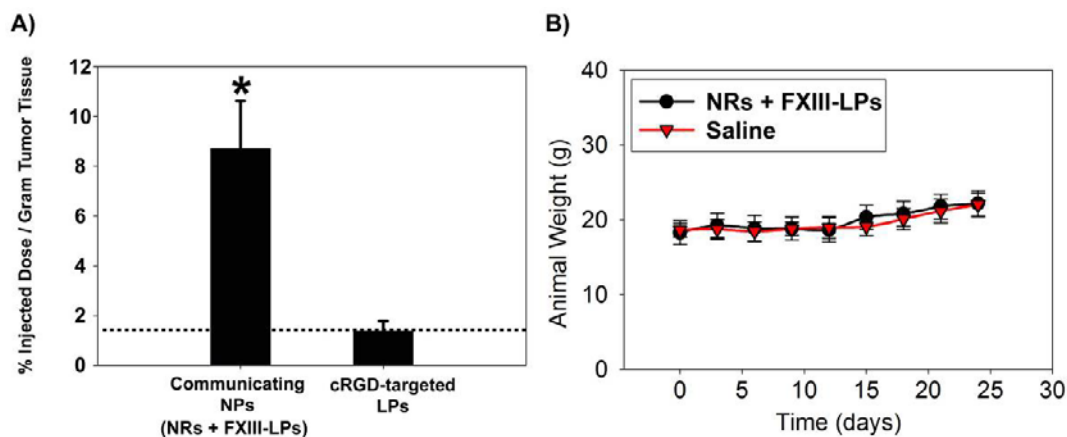
Figure S11. *Therapeutic communicating nanoparticles* **A)** *Comparison between doxorubicin delivery to tumours with communicating LPs and an optimized formulation of cRGD-LPs designed to target the endogenous tumour markers αvβ3 via cyclic RGD peptides.* Communicating NPs (NRs + FXIII-LPs) deliver over 6-fold higher doses of doxorubicin per gram of tumour tissue. **B)** *Animal weights for mice treated with therapeutic nanoparticle systems compared with those administered saline only.*
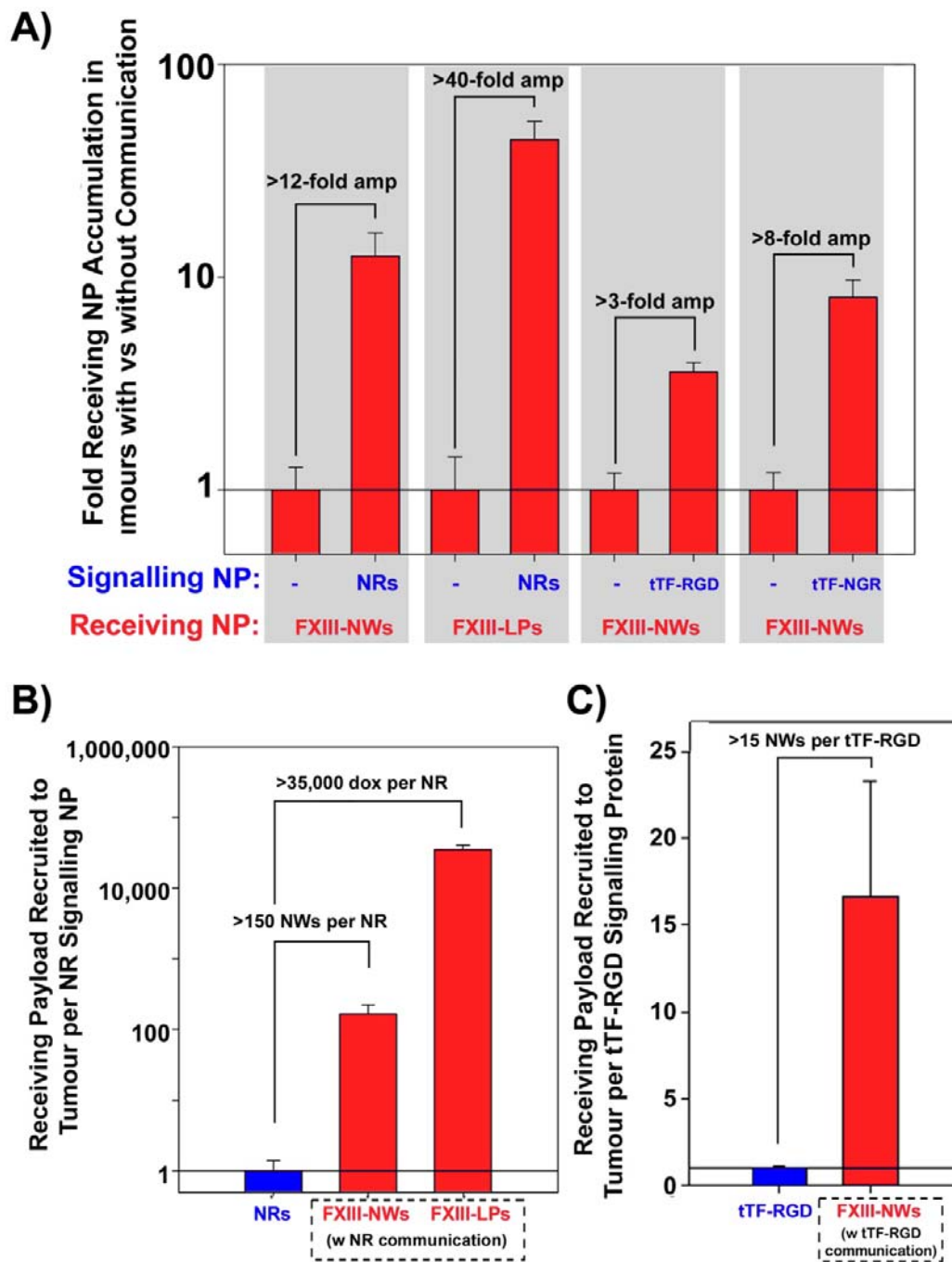
Figure 12. *Probing the ability of communication to amplify Receiving Module localization to tumours.* **A)** *Summary of Receiving Module targeting with vs without communication (tested via exclusion of Signalling NPs).* Data from Figures 4E, 5B, S10A, and S10D were compiled to provide a consolidated comparison of Receiving module targeting to tumours with vs without communication. **B)** *Assessing the amplification achieved during Signalling-to-Receiving communication using NR*

Signalling modules. In order to understand the degree to which NR Signalling modules could recruit multiple Receiving payloads, both diagnostic (iron oxide nanocrystals) and therapeutic (doxorubicin drugs), to tumours, the concentrations of: NR Signalling Modules in tumours (10mg/kg injected dose); FXIII-NWs Receivers in tumours (2 mg/kg, with communication from NRs); and the concentration of doxorubicin (2mg/kg, encapsulated within FXIII-LP Receivers with communication from NRs) were quantified and plotted to display their relative abundance in tumours. In the two systems, respectively, each tumour-localized NR Signalling module was able to recruit >150 NWs or >35,000 doxorubicin molecules from circulation. **C)** *Assessing the amplification achieved during Signalling-to-Receiving module communication using tTF-RGD Signalling modules*. In order to understand the degree to which tTF-RGD Signalling modules could recruit multiple diagnostic (iron oxide nanocrystals) Receiving payloads to tumours, the concentrations of: tTF-RGD Signalling Modules in tumours (25 ug of tTF-RGD per mouse) and FXIII-NW Receivers in tumours (2 mg/kg, with communication from tTF-RGD) were quantified and plotted to display their relative abundance in tumours. In this system, each tumour-localized tTF-RGD was able to recruit >15 NW Receivers from circulation.